

# Towards Determining Amyloid Fibril Structures Using Experimental Constraints from Raman Spectroscopy

Madeline Harper,<sup>1</sup> Uma Nudurupati,<sup>1</sup> Riley J. Workman,<sup>2</sup> Taras I. Lakoba,<sup>3</sup> Nicholas Perez,<sup>1</sup> Delaney Nelson,<sup>1</sup> Yangguang Ou,<sup>1</sup> and David Punihaole\*<sup>1</sup>

<sup>1</sup>Department of Chemistry, University of Vermont, Burlington, Vermont 05405, United States

<sup>2</sup>Sealy Center for Structural Biology and Molecular Biophysics, University of Texas Medical Branch, Galveston, Texas 77555, United States

<sup>3</sup>Department of Mathematics and Statistics, University of Vermont, Burlington, Vermont 05405, United States

(\*Electronic mail: David.Punihaole@uvm.edu)

(Dated: 11 November 2023)

We present structural models for three different amyloid fibril polymorphs prepared from amylin<sub>20–29</sub> (sequence SNN-FGAILSS) and amyloid- $\beta_{25–35}$  (A $\beta_{25–35}$ ) (sequence GSNKGAIIGLM) peptides. These models are based on amide C=O bond and Ramachandran  $\psi$ -dihedral angle data from Raman spectroscopy, which were used as structural constraints to guide molecular dynamics (MD) simulations. The resulting structural models indicate that the basic structural motif of amylin<sub>20–29</sub> and A $\beta_{25–35}$  fibrils are extended  $\beta$ -strands. Our data indicates that amylin<sub>20–29</sub> forms both antiparallel and parallel  $\beta$ -sheet fibril polymorphs, while A $\beta_{25–35}$  forms a parallel  $\beta$ -sheet fibril structure. Overall, our work lays the foundation for using Raman spectroscopy in conjunction with MD simulations to determine detailed molecular-level structural models of amyloid fibrils in a manner that complements gold-standard techniques such as solid-state NMR and cryogenic electron microscopy.

## I. INTRODUCTION

Amyloid fibrils are filamentous,  $\beta$ -sheet-rich protein aggregates that are implicated in numerous diseases, including Alzheimer's, Parkinson's, Huntington's, and Type II Diabetes.<sup>1</sup> Because of their insoluble and non-crystalline nature, conventional structural characterization methods such as X-ray crystallography and solution-state nuclear magnetic resonance (NMR) spectroscopy cannot be used to determine the molecular structure of fibrils.<sup>2</sup> Fortunately, advances in solid-state NMR (ssNMR) and cryogenic electron microscopy (cryo-EM) have enabled the determination of high-resolution structures of amyloid fibrils prepared *in vitro*,<sup>3–6</sup> as well as those harvested from the tissues of patients.<sup>7–12</sup> These studies indicate that fibrils share a common conformational motif known as a “cross- $\beta$ ” structure, in which extended  $\beta$ -sheets stack together with their strands aligned perpendicularly to the fibril's long axis.<sup>13,14</sup> They also demonstrate that fibrils exhibit polymorphism, where a given peptide is capable of forming a variety of distinct fibril structures.<sup>15,16</sup>

Despite the wealth of high-resolution structural information gleaned from ssNMR and cryo-EM, these techniques are not without their pitfalls. Solid-state NMR, for example, requires high sample loads (> 10 mg),<sup>6,17,18</sup> expensive isotopic labeling schemes, and long spectral acquisition times that can take several days.<sup>6</sup> To obtain high-resolution structural data, both ssNMR and cryo-EM require relatively extensive sample preparation to ensure that fibrils are both homogeneous and well-ordered. This can introduce bias in determining the molecular structure of amyloids by preferentially selecting for the most abundant fibril polymorphs. In addition, it can be difficult to resolve electron densities in cryo-EM or obtain good chemical shift dispersion in ssNMR for all but the most well-ordered regions of fibrils. Disordered, dynamic, or structurally heterogeneous regions, which could play impor-

tant roles in initiating aggregation, sequestering other proteins into amyloid plaques, or aberrantly interacting with biological cells, can be difficult to study with these techniques.

In contrast, vibrational methods such as Raman spectroscopy do not suffer from these pitfalls. Raman spectroscopy can be used to interrogate a wide variety of samples with little preparation, including fibrils in solution,<sup>19,20</sup> gels,<sup>21</sup> and fibril films.<sup>22</sup> Data acquisition is relatively fast and robust. In addition, Raman spectroscopy can be used to quantify the distributions of peptide bond and side chain dihedral angles in amyloid fibrils.<sup>21,23–25</sup> Similarly, polarized Raman measurements can be used to determine the relative orientation of chemical bonds and functional groups in fibrils.<sup>22,26</sup> Thus, the conformational sensitivity of Raman spectral features enables the facile differentiation of fibril polymorphs,<sup>21,23,25</sup> as well as the ability to robustly monitor the structural evolution of oligomeric precursors that aggregate into fibrils.<sup>27</sup>

However, despite its versatility and structural sensitivity, Raman spectroscopy is generally considered to be a “low-resolution” characterization method in the broader amyloid community. One reason for this is because Raman spectroscopy has generally only been used to qualitatively evaluate fibril secondary structures rather than determining three-dimensional models like ssNMR. We believe, however, that structural parameters measured using Raman spectroscopy (*vide supra*) can in fact be harnessed to determine detailed molecular-level structural models of amyloid fibrils. We recognize that this can be accomplished by taking inspiration from ssNMR, in which experimentally measured distances and dihedral angles are used as constraints in energy minimization procedures performed on structural models of amyloid fibrils using molecular dynamics (MD) simulations.<sup>18</sup>

To test this idea, we investigated the molecular structures of three fibril polymorphs prepared from amylin<sub>20–29</sub> and amyloid- $\beta_{25–35}$  (A $\beta_{25–35}$ ) peptides. Amylin<sub>20–29</sub>,

which derives from residues 20 – 29 of the 37-amino acid amylin peptide, forms fibrils implicated in the pathology of Type II Diabetes.<sup>28–32</sup> Amyloid- $\beta_{25-35}$  ( $A\beta_{25-35}$ ) derives from residues 25 – 35 of the 40-42 residue long  $A\beta$  peptide.<sup>13,33</sup> Fibrils formed from  $A\beta$  compose extracellular plaques that have been implicated in the pathology associated with Alzheimer’s disease<sup>13,33</sup> and Cerebral Amyloid Angiopathy.<sup>34,35</sup>

## II. EXPERIMENTAL METHODS

### A. Materials

Amylin<sub>20–29</sub> (sequence SNNFGAILSS) and  $A\beta_{25-35}$  (sequence GSNKGAIIGLM) were purchased from GL Biochem (Shanghai, China) at 91% purity and used without further purification. Dimethylsulfoxide (DMSO) was purchased at  $\geq 99.8\%$  purity from Supelco. Milli-Q grade water (18.2 M $\Omega$ cm) was obtained from a Milli-Q<sup>®</sup> IQ 7000 Ultrapure Lab Water System from Millipore Sigma. Phosphate buffer saline tablets were purchased from Sigma Aldrich. Phosphate buffer solution was made from sodium phosphate monobasic monohydrate and sodium phosphate dibasic anhydrous purchased from Fisher Scientific. Filters (0.45  $\mu$ m pore-size) were purchased from Fisher Scientific. Mica (Product No. 50, V1 Grade) and silicon substrates (Product No. 21610 – 55) were purchased from Ted Pella Inc. An ultra-sharp commercial Atomic Force Microscopy (AFM) probe (160AC, OPUS by MikroMach) and a standard AFM probe (PPP-NCHR, Nanosensors<sup>™</sup>) were both purchased from NanoAndMore USA Corporation.

### B. Sample Preparation

Two different fibril polymorphs were prepared from the amylin<sub>20–29</sub> peptide using a modified procedure based on that developed by Madine *et al.*<sup>36</sup> For both polymorphs, 2 mg of peptide were first disaggregated in 20  $\mu$ L of DMSO after incubation at room temperature (22 °C) for 1 h. To prepare the antiparallel  $\beta$ -sheet polymorph (polymorph 1), 980  $\mu$ L of water was slowly added, followed by an additional 1 mL of sodium phosphate buffer (20 mM, pH 7.13). The final solution was 2 mL with a final DMSO concentration of  $1.41 \times 10^{-4}$  mM, 10 mM of buffer, and a peptide concentration of 1.13 mM. To prepare the parallel  $\beta$ -sheet polymorph (polymorph 2), 1980  $\mu$ L of sodium phosphate buffer (100 mM, pH 7.13) was slowly added to the sample. The final solution was 2 mL with a final DMSO concentration of  $1.41 \times 10^{-4}$  mM, 100 mM of buffer, and a peptide concentration of 1.01 mM. The final step for both polymorphs involved filtering solutions using a 0.45  $\mu$ m pore-sized filter to remove any undissolved large aggregates. All starting solutions were visually clear and both samples were incubated at room temperature (22 °C). Aggregates could be visually observed after 7 days of incubation for polymorph 1 and 9 days for polymorph 2.

Parallel  $\beta$ -sheet fibrils were also prepared from  $A\beta_{25-35}$  peptide. This was accomplished by dissolving 2.12 mg of peptide in 1.06 mL of water. The resulting peptide solution appeared visually clear. After this, 1.06 mL of 2 $\times$  phosphate buffer saline (PBS, pH 7.4) was slowly added to the sample for a final peptide concentration of 1 mM. The solution was gently mixed by carefully inverting the sample vial 3 times. Aggregates could be visually observed shortly after preparing the solution and was incubated at 37 °C for 3 days.

### C. Sample Alignment Procedure using Drop Cast Deposition

Following incubation, fibrils were harvested from each sample by centrifuging 500  $\mu$ L of solutions for 1 h at 21300 $\times$ g (Eppendorf Centrifuge 5425). The supernatant for each sample was carefully decanted so that the pellet remained. The pellet was washed twice to remove residual salt crystals by sequentially resuspending it in water and centrifuging. Following this, the pellet was resuspended in 250  $\mu$ L of water. Aliquots of each sample were then diluted, deposited onto a silicon substrate, and allowed to dry in a dust free environment to create a coffee ring<sup>37</sup> for polarized Raman measurements.

### D. Raman Spectroscopy

Raman spectra were measured using a Horiba LabRAM HR Evolution Raman microscope (Horiba Scientific) using 633 nm excitation from a Helium-Neon laser. The laser light was focused on the sample using an infinity-corrected achromatic 100 $\times$  objective (0.9 NA, MPLN100X, Olympus) with the average power ranging from 2.5 mW to 17.9 mW. Acquisition times ranged between 30 – 360 s per spectrum. Spectral acquisition parameters were carefully chosen to balance maximizing signal-to-noise and mitigating photodegradation of samples. Under the illumination conditions used, we observed no visual signs or spectral signatures of sample degradation (Figure S1). Amylin<sub>20–29</sub> polymorph 1 and  $A\beta_{25-35}$  fibril samples exhibited substantial fluorescence backgrounds, which made it difficult to collect high signal-to-noise Raman spectra. The scattered light was collected by the focusing objective in a 180° backscattering geometry. The scattered light was focused into a spectrometer and dispersed using a 600 gr/mm grating. Spectra were imaged using a Synapse EM CCD camera (1600X200-FV, Horiba Scientific).

For polarization measurements, fibrils were aligned so that their long axis was parallel to the polarization of the laser light, which we defined as the laboratory coordinate’s Z direction. The lab frame’s Y coordinate was defined to be along the direction of the laser light’s propagation. A half-wave plate was used to rotate the polarization of the incident light along the X direction, but was removed for incident light polarization measurements involving the Z direction. As described in detail by Adar,<sup>38</sup> this was done to reduce artifacts introduced by the half-wave plate. A polarizer was used to select either the Z or X polarization component of the scattered light, which was then focused into a spectrometer and dispersed us-

ing a 600 gr/mm grating. An optical scrambler was installed before the spectrometer entrance to depolarize the scattered light to minimize the polarization bias of the grating. Polarized Raman measurements were made for the following four incident and scattered light configurations: ZZ, ZX, XZ, and XX (incident and scattered light, respectively).<sup>38</sup> The instrument was benchmarked with Raman polarization measurements of cyclohexane to ensure that our measurements were accurate. We found that the depolarization ratios measured for cyclohexane on our instrument were within experimental error of values reported previously in the literature.<sup>39,40</sup>

### E. Atomic Force Microscopy (AFM)

Samples were prepared for AFM imaging using a procedure that was modified from Ostapchenko *et al.*<sup>41</sup> Briefly, a mica disc was exfoliated to create an atomically flat and clean surface. A 10  $\mu$ L aliquot (2.2 mg/mL) of fibril solution was then deposited onto the disc. The sample was incubated on the disc for 10 min in a dust free environment before being washed 3 $\times$  with water. The sample was then wicked dry with filter paper and dried overnight prior to imaging in a dust free environment.

The AFM measurements were performed on an Asylum MFP-3D-BIO AFM instrument (Oxford Instruments) in the AC mode. Amylin<sub>20–29</sub> polymorph 1 (Figure 1a) was imaged using an ultra-sharp commercial probe with a 26  $\text{Nm}^{-1}$  force constant and 300 kHz resonance frequency. Amylin<sub>20–29</sub> polymorph 2 (Figure 1b) and A $\beta$ <sub>25–35</sub> fibrils (Figure 1c) were imaged using a standard AFM probe with a 42  $\text{Nm}^{-1}$  force constant and 330 kHz resonance frequency.

The images were analyzed with Gwyddion software (open-source software for Scanning Probe Microscopy Data) and the height traces obtained from Gwyddion were visualized as graphs in Graphpad Prism 9. The average diameter for each polymorph was calculated as the maxima of the height trace across 19 or 23 individual fibril fragments (identified visually). See SI for additional details and images (Figure S2).

## III. COMPUTATIONAL METHODS

### A. Molecular Dynamics (MD) Simulations

For the MD simulations, two 24-mer models of amylin<sub>20–29</sub> protofibrils and one 24-mer model of an A $\beta$ <sub>25–35</sub> protofibril were constructed using VMD.<sup>42</sup> For each model, a single  $\beta$ -sheet containing 12 peptides was first built and then duplicated and stacked on the initial  $\beta$ -sheet. The putative fibril structures were constructed based on Raman data. For amylin<sub>20–29</sub>, both an antiparallel and parallel  $\beta$ -sheet fibril model were constructed, while only a parallel  $\beta$ -sheet fibril was constructed for A $\beta$ <sub>25–35</sub>. The  $\alpha$ -carbons of the two stacked  $\beta$ -sheets were initially separated by 10  $\text{\AA}$  for each model. Rather than solvate these models with explicit solvent, we opted to use a generalized Born implicit solvent (GBIS) protocol with a dielectric

constant of 3.23, mimicking that of the interior of proteins, and an ion concentration consistent with experimental sample preparation. Implicit solvent enabled us to better approximate the environment of an effectively infinite fibril. These models consist of 3336 and 3720 atoms for amylin<sub>20–29</sub> and A $\beta$ <sub>25–35</sub> fibrils, respectively.

During the minimization and equilibration simulations, structural constraints obtained from the Raman experimental data were applied to the 24-mer fibril models using NAMD's Collective Variable functionality. In particular, the  $\psi$ -angles of the peptides were harmonically restrained about the  $\psi$ -angle peaks we observe experimentally (150 $^\circ$  amylin<sub>20–29</sub> polymorph 1 and 139 $^\circ$  for amylin<sub>20–29</sub> polymorph 2 and A $\beta$ <sub>25–35</sub>). The angle between peptide carbonyl bonds and the fibril long axis was harmonically constrained to the values obtained experimentally. Additionally, the constraint force constants were tuned to reproduce the experimentally obtained  $\psi$ -angle and C=O bond angle distributions. The fibril axes were approximated in these models by using VMD to calculate the inertial tensor of the  $\alpha$ -carbons and extracting the principal components. The fibril long axes were taken as the resulting principal component perpendicular to the peptides. They were calculated separately for every frame of the simulation trajectories, as atomic fluctuations in the fibrils cause small changes to the axis vectors.

The NAMD MD package was used to energy minimize and simulate the fibril models. The all-atom CHARMM36m force field was used to calculate potential energies and forces due to its improved treatment of secondary structure compared to CHARMM36.<sup>43,44</sup> All simulations were performed under a constant temperature and pressure of 298 K and 1 atm, respectively. The Verlet velocity integration algorithm was used with a time step of 1 fs, and the SHAKE algorithm was employed to constrain heavy atom-hydrogen covalent bonds. Non-bonded interactions were calculated for atom pairs using a cutoff of 12  $\text{\AA}$ , and a switching function was used at distances greater than 10  $\text{\AA}$  to truncate the potential. The particle mesh Ewald method<sup>45</sup> was used to calculate long range electrostatics. Visual and quantitative analysis of MD simulations was performed with Amber's cptraj tool<sup>46,47</sup> and VMD.<sup>42</sup>

The 24-mer fibril models were first energy minimized for 5000 steps with rigid backbone atoms using the conjugate gradient minimization scheme. Following this, we released the rigid backbone atoms and equilibrated the three fibril models for 2 ns with the aforementioned  $\psi$ - and C=O bond angle constraints for each polymorph taken from the Raman data. Following these constrained equilibration simulations, we released all the constraints and ran another 2 ns to observe the thermodynamic stability of the 24-mer fibrils. We collected  $\psi$ - and C=O bond angles, as well as inter-strand and inter-sheet distances from the constrained and unconstrained simulations.

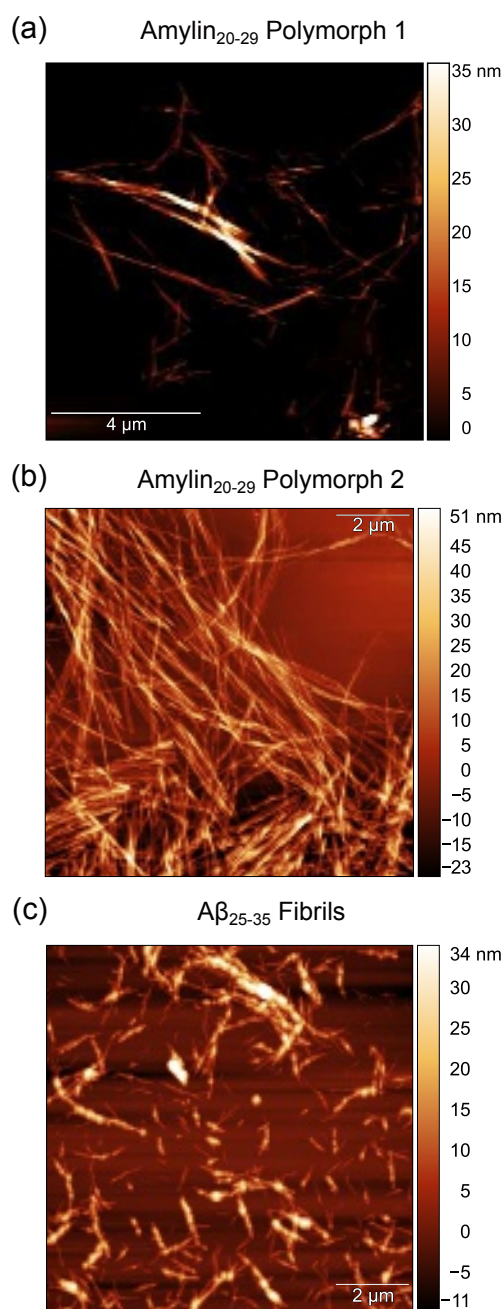


FIG. 1. Representative AFM images of amylin<sub>20–29</sub> and A $\beta$ <sub>25–35</sub> fibrils. (a) AFM image of amylin<sub>20–29</sub> polymorph 1 which is a 256 line image of 10  $\mu\text{m}$   $\times$  10  $\mu\text{m}$  size (4  $\mu\text{m}$  scalebar). (b) AFM image of amylin<sub>20–29</sub> polymorph 2, which is a 512 line image of 10  $\mu\text{m}$   $\times$  10  $\mu\text{m}$  size (2  $\mu\text{m}$  scalebar). (c) AFM image of A $\beta$ <sub>25–35</sub> fibrils, which is a 256 line image of 10  $\mu\text{m}$   $\times$  10  $\mu\text{m}$  size (2  $\mu\text{m}$  scalebar). All images were measured in AC mode. Additional AFM images can be found in the SI (Figure S2).

## IV. RESULTS AND DISCUSSION

### A. Choice of Peptide Systems to Study

We chose to study fibrils prepared from the amylin<sub>20–29</sub> and A $\beta$ <sub>25–35</sub> peptides because of their small, tractable nature, which makes them ideal for quantitatively analyzing Raman spectra without the need for complex isotopic labeling schemes and performing detailed MD simulations. Studies suggest that residues 20 – 29 form the amyloidogenic core of amylin.<sup>48–50</sup> Fibrils prepared from amylin<sub>20–29</sub> can be poised to adopt well-defined morphologies,<sup>51–54</sup> but there have been conflicting reports on whether it forms parallel, antiparallel, or mixed  $\beta$ -sheet fibril structures.<sup>36,52–54</sup> Wildtype A $\beta$  consists of two predominate isoforms, the 40-residue A $\beta$ <sub>1–40</sub> and the 42-residue A $\beta$ <sub>1–42</sub>. Although it is a less abundant isoform, A $\beta$ <sub>25–35</sub> has also been found in the brain<sup>55</sup> and has been shown to aggregate into  $\beta$ -sheet structures.<sup>56–59</sup> Despite this, we are unaware of any known structures reported for A $\beta$ <sub>25–35</sub> fibrils.

### B. AFM Imaging

AFM imaging (Figure 1) reveals that the aggregated samples prepared from amylin<sub>20–29</sub> and A $\beta$ <sub>25–35</sub> peptides resulted in the formation of amyloid fibrils. The two polymorphs produced from amylin<sub>20–29</sub> (Figure 1a, b) exhibit similar morphologies, consisting of unbranched fibrils that are several microns in length. In contrast, the fibrils prepared from A $\beta$ <sub>25–35</sub> are shorter, being only several hundred nanometers to a few microns in length.

### C. Raman Spectroscopy Analysis

To further characterize the fibrils, we used Raman spectroscopy to investigate their molecular structures. As shown in Figure 2, each polymorph exhibits unique spectral fingerprints in the region between 1100 – 1700  $\text{cm}^{-1}$ . The most structurally informative Raman bands in the spectra occur in the Amide I, II, and III regions, located between 1600 – 1700  $\text{cm}^{-1}$ , 1500 – 1600  $\text{cm}^{-1}$ , and 1200 – 1350  $\text{cm}^{-1}$ , respectively. We examined these regions in detail to obtain structural information about the fibrils by performing spectral deconvolution analysis (see SI for details, Figures S4 and S5). The results of this analysis are summarized in Table I, which lists the Raman band assignments for the three polymorphs.

The most intense features in the spectra shown in Figure 2 occur in the Amide I region. The Amide I vibration consists mainly of amide C=O stretching.<sup>63</sup> Its structural sensitivity derives from transition dipole coupling between neighboring C=O oscillators that produce a delocalized Amide I normal mode.<sup>61,65,67–70</sup> Coupling also results in characteristic “excitonic splitting” patterns in the Amide I band that are diagnostic of different protein secondary structure elements. For example, the Amide I band for canonical (infinitely long) parallel  $\beta$ -sheets is predicted to split into two sub-bands, a high

TABLE I. Band frequencies and assignments for the Amide I, II, and III regions of amylin<sub>20–29</sub> and A $\beta$ <sub>25–35</sub> fibrils

Amylin <sub>20–29</sub> (cm <sup>-1</sup> ) <sup>a</sup>		A $\beta$ <sub>25–35</sub> (cm <sup>-1</sup> ) <sup>a</sup>	Band assignment <sup>c</sup>	Reference
Polymorph 1	Polymorph 2			
1207	1207	–	Phe phenyl-C str	Asher <i>et al.</i> <sup>60</sup>
1220	–	1213	CH b, heavily mixed with NH ipb, CN str	Moore & Krimm <sup>61</sup>
1236	1225	1225	Amide III <sub>3</sub> of fibrils	Mikhonin <i>et al.</i> <sup>62</sup> , Punihaole <i>et al.</i> <sup>21</sup>
–	1241	1253	Amide III <sub>3</sub> of non-fibrillar species	Mikhonin <i>et al.</i> <sup>62</sup>
1282 <sup>b</sup>	1282	1279	CH b, heavily mixed with NH ipb, CN str	Moore & Krimm <sup>61</sup>
–	1555	1557 <sup>b</sup>	Amide II	Barth <sup>63</sup>
–	1586	–	Phe CC ring str	Barth <sup>64</sup>
1605	1606	–	Phe ip ring str/ Phe CC ring str	Asher <i>et al.</i> <sup>60</sup> , Barth <sup>64</sup>
1633 <sup>b</sup>	1630	1623	Amide I B of fibrils	Moore & Krimm <sup>61,65</sup>
–	1653	–	Amide I of non-fibrillar aggregates	Maiti <i>et al.</i> <sup>20</sup> , Apetri <i>et al.</i> <sup>27</sup>
1671	1670	1671	Amide I A of fibrils	Moore & Krimm <sup>61,65</sup>
–	1677	–	Amide I of non-fibrillar aggregates	Maiti <i>et al.</i> <sup>20</sup>

<sup>a</sup>unless otherwise noted, the uncertainty is  $\pm 1$  cm<sup>-1</sup>; <sup>b</sup>uncertainty is  $\pm 3$  cm<sup>-1</sup>; <sup>c</sup>ip: in-plane; b: bending; str: stretching.

frequency  $A(0,0)$  mode and a low frequency  $B(\pi,0)$  mode that are both Raman and IR-active.<sup>71–73</sup> In contrast, the Amide I band is predicted to split into four sub-bands for canonical (infinitely long) antiparallel  $\beta$ -sheet structures: the  $A(0,0)$  mode, which is Raman-active and forbidden in the IR; the  $B_1(0,\pi)$  mode, which is relatively weak in both Raman and IR; the  $B_2(\pi,0)$  mode, which is very strong in IR spectra; and the  $B_3(\pi,\pi)$ , which is essentially forbidden in IR and Raman spectra.<sup>71–73</sup> In practice, however, it can be difficult to differentiate between parallel and antiparallel  $\beta$ -sheet structures using the Amide I band alone.<sup>74</sup> This is because the Amide I band depends on additional factors such as hydrogen bonding patterns of the peptide bond C=O groups, the registry of  $\beta$ -strands, and the twist of the  $\beta$ -sheets.<sup>63,75–77</sup>

The intense band at ca. 1670 cm<sup>-1</sup> can be assigned to the Amide I  $A(0,0)$  for all polymorphs. The  $B(\pi,0)$  mode occurs near 1630 cm<sup>-1</sup> for both amylin<sub>20–29</sub> polymorphs and is downshifted to ca. 1620 cm<sup>-1</sup> in A $\beta$ <sub>25–35</sub> fibrils. We do not observe Raman bands in any of the fibril spectra that can be assigned to the  $B_1(0,\pi)$  mode characteristic of canonical antiparallel  $\beta$ -sheet structures. However, for amylin<sub>20–29</sub> polymorph 1, we observe a band at 1695 cm<sup>-1</sup> in the IR spectrum (Figure S6), which we assign to the  $B_1(0,\pi)$  mode. The presence of this band suggests that these fibrils are composed of antiparallel  $\beta$ -sheet structures (*vide infra*). We attribute the absence of the  $B_1(0,\pi)$  mode in the Raman spectrum to the fact that there is likely some local disordering of the  $\beta$ -strand registries in the amylin<sub>20–29</sub> polymorph 1 fibrils.

Spectral deconvolution analysis of the Amide I region of amylin<sub>20–29</sub> fibrils (Figure S4a,b) suggests the presence of additional structures for polymorph 2 (Figure S4b). As discussed in detail in the SI, modeling the Amide I region between ca. 1600 – 1700 cm<sup>-1</sup> of polymorph 2 with just two bands (the Amide I A and B modes) yields a poor fit (Figure S4c). In addition, adding only the 1677 cm<sup>-1</sup> band improves the fit, but the Amide I B bandwidth becomes unphysically large (Figure S4d). The most parsimonious, satisfactory, and physically reasonable fit that we obtain is by incorporating two additional bands at 1653 cm<sup>-1</sup> and 1677 cm<sup>-1</sup> into the fit.

As discussed in detail below, we assign these bands to Amide I modes deriving from  $\alpha$ -helical (1653 cm<sup>-1</sup>)<sup>20,27</sup> and PPII-like structures (1677 cm<sup>-1</sup>) from non-fibrillar aggregates present in the sample.<sup>20</sup>

The amylin<sub>20–29</sub> fibrils contain additional bands in the ca. 1600 – 1700 cm<sup>-1</sup> region. Both amylin<sub>20–29</sub> polymorphs exhibit bands at ca. 1605 cm<sup>-1</sup>, while polymorph 2 exhibits an additional band at 1586 cm<sup>-1</sup>. These bands can be assigned to the in-plane ring stretching modes of phenylalanine (Phe).<sup>60,64</sup> For amylin<sub>20–29</sub> polymorph 2, these bands exhibit narrow linewidths, which we attribute to the Phe rings adopting more well-defined conformations compared to polymorph 1 (*vide infra*). Amylin<sub>20–29</sub> fibrils are also expected to contain spectral contributions from asparagine's (Asn) side chain C=O stretching mode.<sup>24,78,79</sup> We see no evidence that the Asn residues of amylin<sub>20–29</sub> fibrils contribute significant spectral contributions to the 1600 – 1700 cm<sup>-1</sup> region. However, to confirm that our assignment of ca. 1670 cm<sup>-1</sup> bands in amylin<sub>20–29</sub> fibrils is correct, we measured the Raman spectrum of a lyophilized powder of Asn. The Raman spectrum of Asn (Figure S7) exhibits a strong band at 1640 cm<sup>-1</sup>, which can be assigned to the C=O stretching mode of Asn side chains. This suggests that the spectral contributions of Asn side chains is negligible for the ca. 1670 cm<sup>-1</sup> bands that we assign to the Amide I  $A(0,0)$  of the peptide backbone amide groups.

The Amide II mode gives rise to a band located in the 1500 – 1600 cm<sup>-1</sup> region. It consists of an out-of-phase combination of NH in-plane bending and CN stretching. The Amide II is typically strong in IR spectra, but weak in Raman spectra excited with visible wavelengths. Interestingly, Lee and coworkers<sup>19</sup> suggest that the Amide II is enhanced in the Raman spectra of parallel  $\beta$ -sheet structures. As seen in Figure 2, the Amide II is suppressed in the spectrum of amylin<sub>20–29</sub> polymorph 1 (Figure 2a), but appears in the spectra of the other two fibril polymorphs (Figure 2b-c). This suggests that amylin<sub>20–29</sub> polymorph 2 and A $\beta$ <sub>25–35</sub> fibrils consist of parallel  $\beta$ -sheet structures.

The most structurally-sensitive bands in the Raman spectra

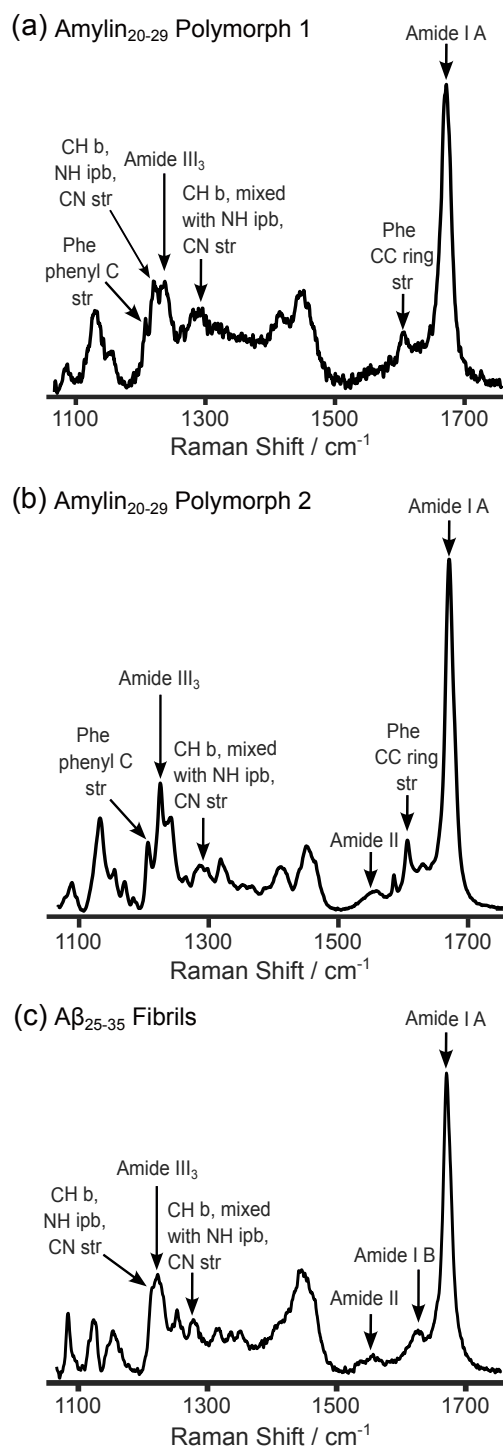


FIG. 2. Raman spectra of amylin<sub>20-29</sub> and A $\beta$ <sub>25-35</sub> fibrils. (a) Amylin<sub>20-29</sub> polymorph 1 fibrils. (b) Amylin<sub>20-29</sub> polymorph 2 fibrils. (c) A $\beta$ <sub>25-35</sub> fibrils. All spectra were smoothed with a Savitzky-Golay Filter<sup>66</sup> using a 4<sup>th</sup> order polynomial over an 11-point window for visual clarity. The original spectra can be found in Figure S3.

shown in Figure 2 occur between ca. 1200–1350 cm<sup>-1</sup> in the Amide III region. The canonical Amide III band, as characterized in N-methylacetamide, occurs at ca. 1315 cm<sup>-1</sup> and

originates from a vibration consisting of an in-phase combination of NH in-plane bending and CN stretching.<sup>80</sup> In peptides and proteins, however, the Amide III region is considerably more complex, consisting of several bands that derive from vibrations containing significant contributions of CN stretching, NH bending, and/or C $\alpha$ H bending motions. Asher and coworkers,<sup>81</sup> have assigned the Amide III region of peptides and proteins in detail, identifying three sub-bands called the Amide III<sub>1</sub>, Amide III<sub>2</sub>, and Amide III<sub>3</sub>. They have shown that the Amide III<sub>3</sub> is the most conformationally sensitive,<sup>62</sup> as its frequency can be correlated to the Ramachandran  $\psi$ -dihedral angles of peptide bonds.<sup>62,82</sup>

For  $\beta$ -sheet structures, the Amide III<sub>3</sub> band occurs between ca. 1220–1240 cm<sup>-1</sup>, and it is easily identified due to its relatively strong intensity (even with visible Raman excitation) compared to other bands in the region.<sup>83</sup> Based on peak intensities from our spectral deconvolution analysis (Figures S4 and S5), we assign the 1236 cm<sup>-1</sup> band for amylin<sub>20-29</sub> polymorph 1, 1225 cm<sup>-1</sup> band for amylin<sub>20-29</sub> polymorph 2, and the 1225 cm<sup>-1</sup> band for A $\beta$ <sub>25-35</sub> fibrils to Amide III<sub>3</sub> modes that are diagnostic of amyloid fibril  $\beta$ -sheet structures.<sup>21,23,25,84</sup>

We capitalized on the structural sensitivity of the Amide III<sub>3</sub> band to determine the distribution of Ramachandran  $\psi$ -angles for the amylin<sub>20-29</sub> and A $\beta$ <sub>25-35</sub> fibril peptide bonds. To do this, we utilized the methodology of Asher and coworkers,<sup>85</sup> which correlates the frequencies of the Amide III<sub>3</sub> band envelope to different  $\psi$ -angles (see SI for details). As shown in Figure 3, the  $\psi$ -angles for all the fibril polymorphs occur between ca. 120–160°. The distribution for amylin<sub>20-29</sub> polymorph 1 (Figure 3a) is centered at 151°, well within the range of canonical antiparallel  $\beta$ -sheet structures.<sup>86</sup> In contrast, the distributions for the other polymorphs are centered at ca. 140° (Figure 3b-c), indicating that they are composed of parallel  $\beta$ -sheet structures.<sup>86</sup> Based on its narrower  $\psi$ -angle distribution width, amylin<sub>20-29</sub> polymorph 2 fibrils exhibit a more well-defined conformation than amylin<sub>20-29</sub> polymorph 1 or A $\beta$ <sub>25-35</sub> fibrils. Additionally, we observe no  $\psi$ -angle populations in the fibrils that suggest there are  $\beta$ -turn structures. This indicates that all three polymorphs consist of extended  $\beta$ -strands that assemble into  $\beta$ -sheets.

We observe additional Amide III<sub>3</sub> bands between ca. 1240–1250 cm<sup>-1</sup> for amylin<sub>20-29</sub> polymorph 2 and A $\beta$ <sub>25-35</sub> fibrils. The frequencies of these bands are upshifted beyond the range that is typical of amyloid  $\beta$ -sheet structures and likely derive from non-fibrillar aggregates that we observe in some of the AFM images for these two polymorphs (Figure S2c-f). These bands correspond to  $\psi$ -angle distributions centered at either 156° (168°) or -28° (-40°) for amylin<sub>20-29</sub> polymorph 2 (A $\beta$ <sub>25-35</sub>) fibrils (Figure S8). Based on our assignments of the Amide I bands at 1653 cm<sup>-1</sup> and 1677 cm<sup>-1</sup> (*vide supra*), the  $\psi$ -angle distributions for amylin<sub>20-29</sub> polymorph 2 centered at 156° and -28° likely derive from  $\alpha$ -helical and PPII-like/disordered structures, respectively. In contrast, our analysis of the Amide I region for A $\beta$ <sub>25-35</sub> fibrils suggests that there are no  $\alpha$ -helical or disordered structures present (Figure S5). Thus, the Amide III<sub>3</sub> band located at 1253 cm<sup>-1</sup> likely corresponds to non-fibrillar aggregates that

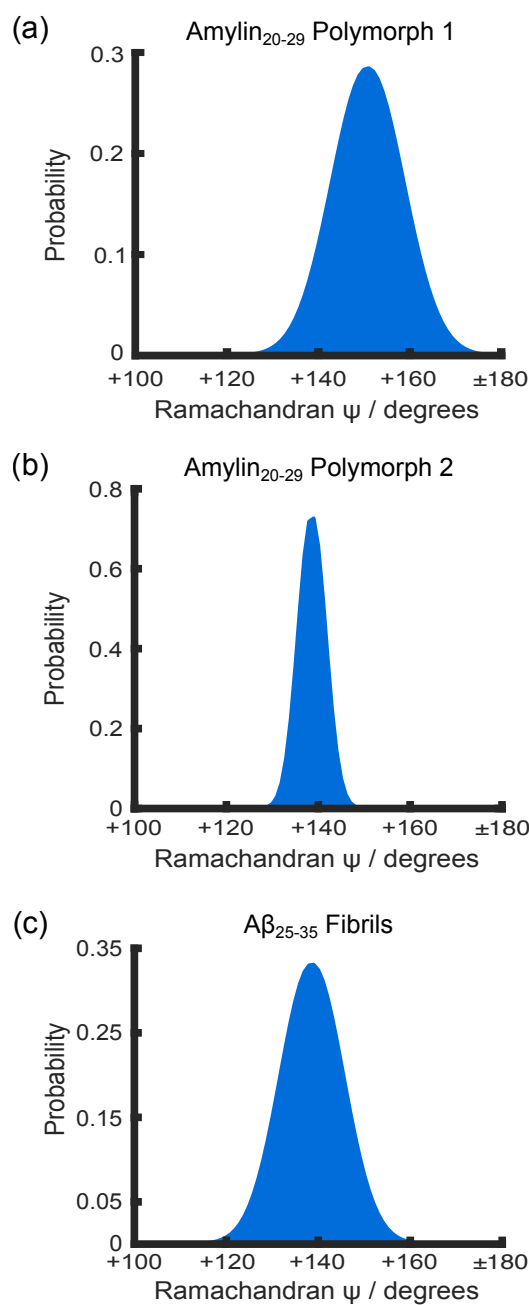


FIG. 3. Ramachandran  $\psi$ -angle distribution determined from the Amide III<sub>3</sub> mode for amylin<sub>20-29</sub> and A $\beta_{25-35}$  fibrils. (a) Amylin<sub>20-29</sub> polymorph 1 Ramachandran  $\psi$ -angle distribution with a mean  $\psi$ -angle of 151°. (b) Amylin<sub>20-29</sub> polymorph 2 Ramachandran  $\psi$ -angle distribution with a mean  $\psi$ -angle of 139°. (c) A $\beta_{25-35}$  fibrils Ramachandran  $\psi$ -angle distribution with a mean  $\psi$ -angle of 139°. The distributions indicate that the cross- $\beta$  core structure of (a) is composed of extended  $\beta$ -strands oriented in an antiparallel  $\beta$ -sheet while (b) and (c) are composed of extended  $\beta$ -strands oriented in an  $\beta$ -parallel sheet.

are rich in  $\beta$ -strand-like structures with  $\psi$ -angles centered at  $-168^\circ$ .

#### D. Polarized Raman Measurements

We used polarized Raman spectroscopy to gain additional structural insights on amylin<sub>20-29</sub> and A $\beta_{25-35}$  fibrils. Raman anisotropy measurements on aligned samples can be employed to determine the relative orientation of chemical bonds and functional groups in fibrils, as first demonstrated by Lednev and coworkers.<sup>22</sup> We prepared anisotropic samples of aligned fibrils for each polymorph using a drop coat deposition method.<sup>22,37</sup> This method creates a “coffee ring” peptide film that forms because the evaporation of the solvent produces shear forces that move fibrils in the center of the droplet towards the perimeter.<sup>37</sup> As the fibrils approach the perimeter of the droplet, they align themselves parallel to its edge with a high degree of ordering.<sup>87</sup>

We aligned the incident laser light to the edge of the coffee ring for the polarized Raman measurements. We designated a laboratory coordinate system (XYZ) where the Z-direction corresponds to the long axis of the fibrils (tangent to the coffee ring edge) and the Y-axis to the propagation direction of the incident laser light (Figure 4 inset). Given the uniaxial symmetry of the fibrils, we only needed to acquire Raman spectra using four different combinations of incident and scattered light polarization configurations to obtain orientation information of chemical functional groups: ZZ, ZX, XZ, and XX (where the first and second letter indicate the direction of the incident and scattered light, respectively, along the laboratory coordinate system).<sup>38</sup>

The polarized Raman spectra of the three different fibril polymorphs are shown in Figure 4. As expected, the cross-polarized spectra (ZX and XZ, shown in blue and purple, respectively) overlap almost perfectly, indicating that there is no photodamage of the samples, no artifacts introduced by the different configurations of the polarization optics used (see Experimental Methods for more details), and that no displacements/rotations occurred in the samples during the measurement. The ZZ (black) and XX (red) spectra show the largest intensity variations. The most striking difference occurs with the Amide I A(0,0) band, which is most intense in the ZZ spectrum and very weak in the XX spectrum.

Quantitatively interpreting the polarized spectra to extract orientation information requires knowing the Raman tensors for particular vibrational normal modes. Fortunately, the Raman tensor for the (delocalized) Amide I A(0,0) mode has been determined. It is oriented parallel to the C=O axis of peptide bonds in  $\beta$ -sheet structures.<sup>88</sup> Thus, the Amide I A(0,0) band is an ideal spectroscopic marker to determine the relative orientation of C=O bonds in amylin<sub>20-29</sub> and A $\beta_{25-35}$  fibrils.

The theory to obtain orientation information from polarized Raman spectra has been described in extensive detail elsewhere.<sup>89-92</sup> The key step is to determine the respective most probable orientation distribution functions,  $N_{mp}(\theta)$ , for the Amide I A(0,0) tensor of each polymorph. The method of finding  $N_{mp}(\theta)$  is described in the section *Basic Approach to Determine the Most Probable Orientation Distribution Function* of the SI. Briefly, for systems such as fibrils with uniaxial symmetry,  $N_{mp}(\theta)$  can be estimated with

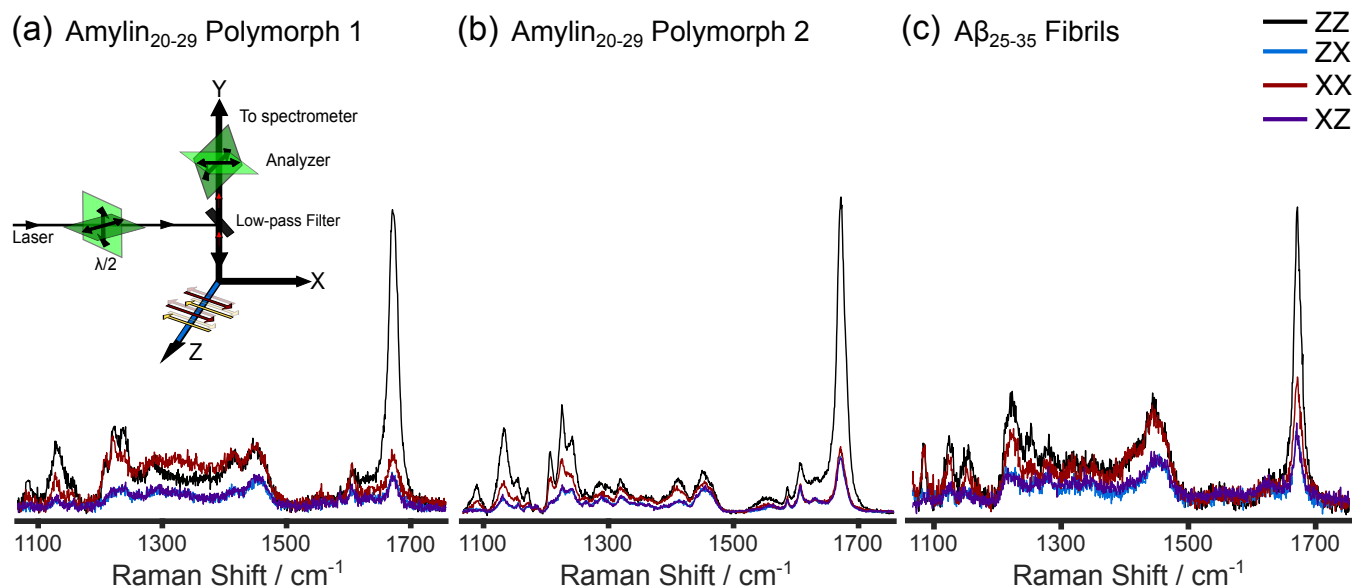


FIG. 4. Polarized Raman spectra of amylin<sub>20-29</sub> and A $\beta$ <sub>25-35</sub> fibrils. (a) Amylin<sub>20-29</sub> polymorph 1. (a, inset) Schematic of polarization configurations. (b) Amylin<sub>20-29</sub> polymorph 2. (c) A $\beta$ <sub>25-35</sub> fibrils. The spectra shown here have not been smoothed.

reasonable accuracy by experimentally measuring two order parameters called  $\langle P_2 \rangle$  and  $\langle P_4 \rangle$ .<sup>93</sup> As discussed in detail in the SI, these order parameters can be determined from the intensity ratios  $R_1 = I_{ZZ}/I_{ZZ}$  and  $R_2 = I_{XZ}/I_{XX}$  for the Amide I  $A(0,0)$  mode (see Table S1 and S2 and Figures S9-S17).<sup>89</sup>

Figure 5a-c shows  $N_{mp}(\theta)$  for the Amide I  $A(0,0)$  tensors. The distributions are normalized such that multiplying  $N_{mp}(\theta)$  by  $\sin \theta$  yields the preferred orientation distribution of the tensors. As shown in Figure 5d-f, preferred orientation distributions of the Amide I  $A(0,0)$  tensors for all the polymorphs are bimodal. The maximum probability for the distributions corresponding to the Amide I  $A(0,0)$  tensors occur at ca.  $\pm 10^\circ$  and  $\pm 15^\circ$  for amylin<sub>20-29</sub> polymorphs 1 and 2, respectively, and  $\pm 11^\circ$  for A $\beta$ <sub>25-35</sub> fibrils (Table II). These values indicate that the  $\beta$ -strands of the polymorphs are oriented approximately perpendicularly to the fibril long axis, which is the hallmark of the cross- $\beta$  architecture observed in amyloids. The smaller peaks in the C=O bond angle distributions that occur at  $90^\circ$  can be attributed to local disordering of the cross- $\beta$  structure or because of misalignment of the fibril filaments in the coffee rings that we prepared. Based on the relative intensities of the peaks, disordering and misalignment accounts for roughly 19% for both amylin<sub>20-29</sub> polymorphs and 33% for A $\beta$ <sub>25-35</sub> fibrils of the total probability for the C=O bond angle distributions.

#### E. Determining Force Constants for Harmonic Constraints.

The widths of the experimentally measured C=O and  $\psi$ -angle distributions can be used to determine harmonic constraints that can be applied in MD simulations. For example, the probabilities of the experimentally measured  $\psi$ -angles can

be modeled using the Boltzmann distribution:

$$\frac{p(\psi_i)}{p(\psi_{eq})} = e^{-\Delta G(\psi_i)/RT} \quad (1)$$

where  $p(\psi_i)/p(\psi_{eq})$  is the ratio of peptide bonds with  $\psi$ -angles  $\psi_i$  and  $\psi_{eq}$ , respectively. The angle,  $\psi_{eq}$ , is the “equilibrium” or minimum energy  $\psi$ -angle for each polymorph, while  $R$  is the molar gas constant,  $T$  is the temperature, and  $\Delta G(\psi_i) = G(\psi_i) - G(\psi_{eq})$  is the apparent Gibbs free energy difference between  $\psi_i$  and  $\psi_{eq}$ . From eq. 1,  $\Delta G(\psi_i)$ , can be determined:

$$\Delta G(\psi_i) = -RT \ln \left[ \frac{p(\psi_i)}{p(\psi_{eq})} \right] \quad (2)$$

Eq. 2 can be used to determine an apparent free energy landscape for the fibril peptide bonds along the  $\psi$ -angle structure coordinate. As shown in Figure 6, the apparent energy landscapes behave harmonically around  $\psi_{eq}$  and can be modeled in terms of a simple torsional spring using Hooke’s Law:<sup>24</sup>

$$\Delta G(\psi_i) = \frac{1}{2} \kappa (\psi_i - \psi_{eq})^2 \quad (3)$$

where  $\kappa$  is the torsional spring force constant, which reflects the curvature of the harmonic potential wells. A similar approach can also be used to determine the torsional spring constants for the C=O bond angles. These distributions are more complex, and, as shown in Figure 7, the potential energy landscapes are anharmonic. To calculate the force constants, however, we assume that the potential wells behave harmonically

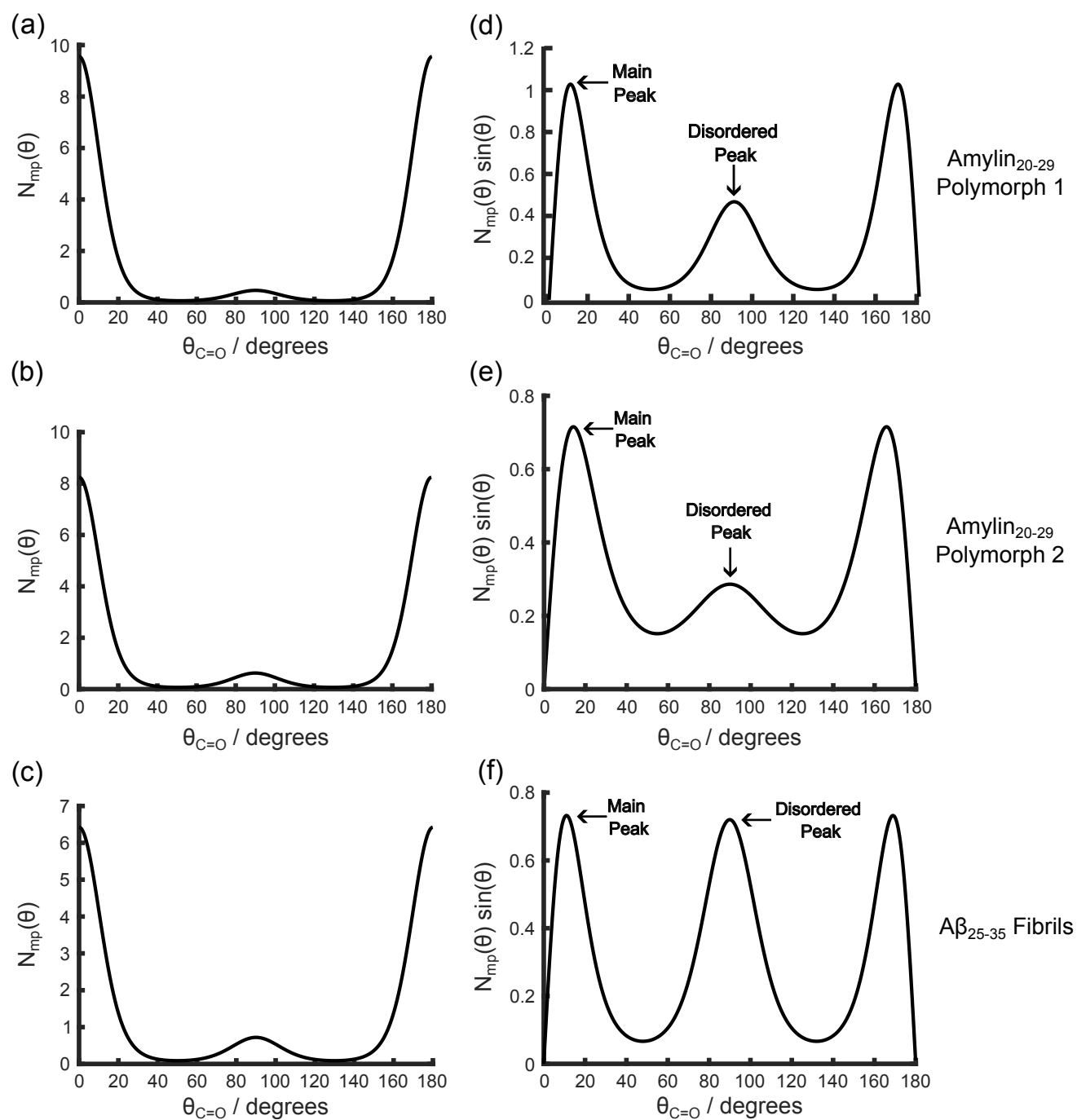


FIG. 5. The most probable orientation distribution function (a-c),  $N_{mp}(\theta)$ , and the preferred orientation distribution (d-f),  $N_{mp}(\theta) \sin(\theta)$ , for the Amide I  $A(0,0)$  Raman tensors for amylin<sub>20-29</sub> and  $A\beta_{25-35}$  fibril polymorphs.  $\theta$  defines the angle of the tensor or bond with respect to the long axis of the fibril. (a, d) Amylin<sub>20-29</sub> polymorph 1, (b, e) Amylin<sub>20-29</sub> polymorph 2, (c, f)  $A\beta_{25-35}$  fibrils.

TABLE II. Summary of Raman-derived structural constraints for amylin<sub>20-29</sub> and  $A\beta_{25-35}$  fibrils

	$\beta$ -sheet	$\psi$ angle ( $^\circ$ )	$\kappa$ for $\psi$ (J/mol/deg)	C=O bond angle ( $^\circ$ )	$\kappa$ for C=O (J/mol/deg)
Amylin <sub>20-29</sub> Polymorph 1	Antiparallel	151	40.54	$\pm 10$	43.07
Amylin <sub>20-29</sub> Polymorph 2	Parallel	139	258.6	$\pm 15$	18.63
$A\beta_{25-35}$ fibrils	Parallel	139	52.67	$\pm 11$	32.72

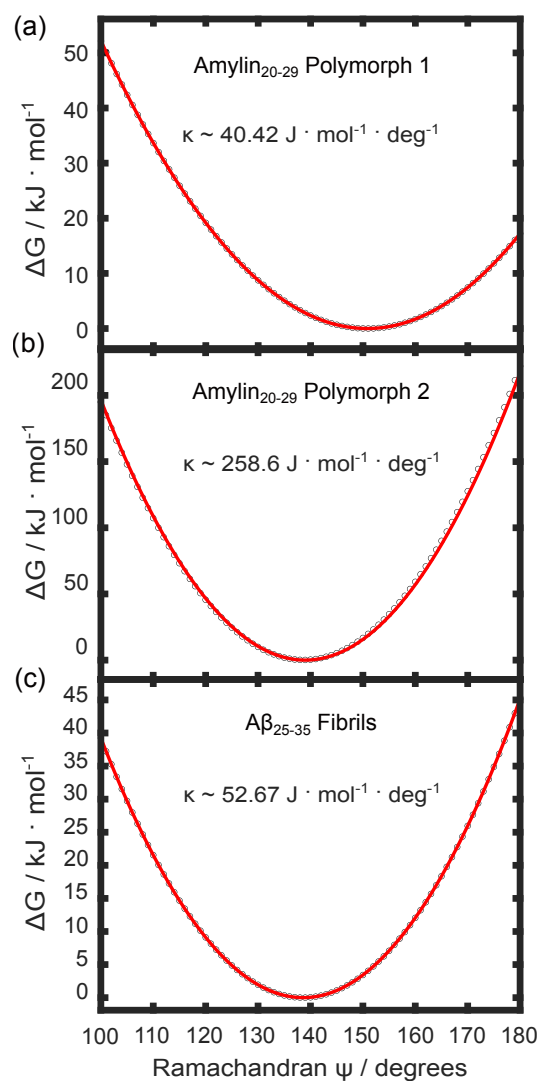


FIG. 6. Apparent Gibbs Free energy landscapes (shown in black circles) for amylin<sub>20–29</sub> and A $\beta$ <sub>25–35</sub> fibrils Ramachandran  $\psi$ -angle. The energy wells can be modeled by assuming a harmonic oscillator torsional spring near the equilibrium angles (shown in red). (a) Amylin<sub>20–29</sub> polymorph 1. (b) Amylin<sub>20–29</sub> polymorph 2. (c) A $\beta$ <sub>25–35</sub> fibrils.

in the region between 5 – 20°, near the equilibrium bond angles.

Table II summarizes the force constants obtained from the experimentally measured  $\psi$ - and C=O angle distributions. It is important to note that fibril misalignment introduces additional uncertainty in determining the force constants for the C=O bond angles, but not the Ramachandran  $\psi$ -angles. The effect of this greater uncertainty is that the apparent force constants determined experimentally for the C=O bond angles are lower than in actuality. This means that the structural constraints applied in the MD simulations are relaxed and allows a greater ensemble of fibril structures to be sampled in the trajectories, effectively reducing the apparent resolution of our

structural models.

#### F. Guided MD Simulations using Experimental Constraints from Raman Spectroscopy.

We recognized that the C=O and  $\psi$ -angle distributions obtained from Raman measurements provide structural constraints that can be used to determine molecular structural models of the amylin<sub>20–29</sub> and A $\beta$ <sub>25–35</sub> fibril polymorphs. To accomplish this, we first manually constructed putative structural models of the three different fibril polymorphs for MD simulations. These initial models were constructed by arranging 24 peptides in a two  $\beta$ -sheets comprised of 12 peptides per sheet. Using the Raman data as a guide, we constructed  $\beta$ -sheets comprised of only extended  $\beta$ -strands that were arranged in an antiparallel configuration for amylin<sub>20–29</sub> polymorph 1 and parallel configurations for amylin<sub>20–29</sub> polymorph 2 and A $\beta$ <sub>25–35</sub> fibrils. When initially constructing these models, we only considered  $\beta$ -sheet structures wherein the strands were in-register and explicitly solvated these structural models in TIP3P<sup>94</sup> before performing energy minimization and equilibration runs. Upon performing the equilibration runs, we found that the A $\beta$ <sub>25–35</sub> model was structurally unstable since water molecules penetrated the interior of the  $\beta$ -sheet and formed strong dipole-charge interactions with the lysine (Lys) side chains.

Because of this, we employed a generalized-Born implicit solvent with a dielectric constant set to 3.23 (appropriate for the interiors of proteins)<sup>95</sup> for all three structural models. We reasoned that the use of implicit solvent was physically reasonable for our simulations since it better mimics the bulk properties of real fibril systems that were examined experimentally compared to the small, well-solvated  $\beta$ -sheet oligomers in the explicit solvent simulations. However, following the equilibration of these GBIS solvated models, we found that the A $\beta$ <sub>25–35</sub> structure was still not thermodynamically stable. Upon analysis of this structure, we observed that the in-register arrangement of the  $\beta$ -strands resulted in repulsive electrostatic interactions of Lys side chains, which caused the  $\beta$ -sheets to dissociate. To alleviate this problem, we offset the  $\beta$ -strands in the sheets by one residue. We found that this resulted in thermodynamically stable structures, as it allowed the Lys residues to form favorable hydrogen bonds with the nearby Asn and serine (Ser) side chains (*vide infra*), rather than the repulsive interactions that we previously observed.

Using an analogous approach to ssNMR, we restrained the C=O and  $\psi$ -angles of the fibril models during the energy minimization and equilibration simulation runs using the equilibrium angles and torsional force constants determined experimentally from our Raman measurements. Figure 8 presents representative snapshots from the resulting ensemble of fibril structures for the three polymorphs from the MD simulations that are consistent with the experimental data from the Raman measurements. All three polymorphs are composed of extended  $\beta$ -strands that assemble into sheets. The strands for amylin<sub>20–29</sub> polymorph 1 assemble into antiparallel  $\beta$ -sheets, while those of polymorph 2 and A $\beta$ <sub>25–35</sub> form parallel  $\beta$ -sheet

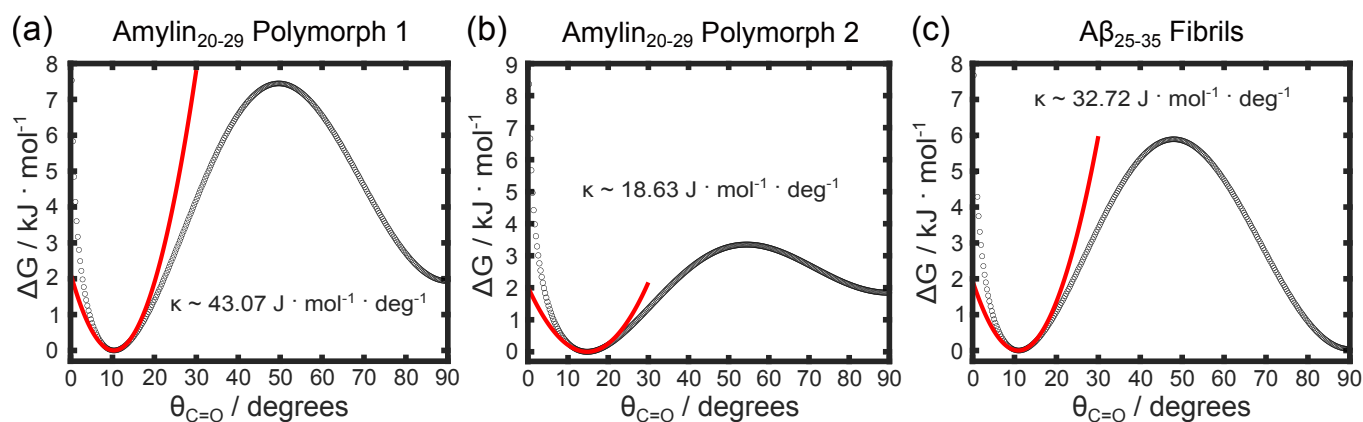


FIG. 7. Apparent Gibbs Free energy landscapes (shown in black circles) for amylin<sub>20–29</sub> and A $\beta$ <sub>25–35</sub> polymorph C=O bond angles. The energy wells can be modeled by assuming a harmonic oscillator model torsional spring near the equilibrium angles (shown in red). (a) Amylin<sub>20–29</sub> polymorph 1. (b) Amylin<sub>20–29</sub> polymorph 2. (c) A $\beta$ <sub>25–35</sub> fibrils.

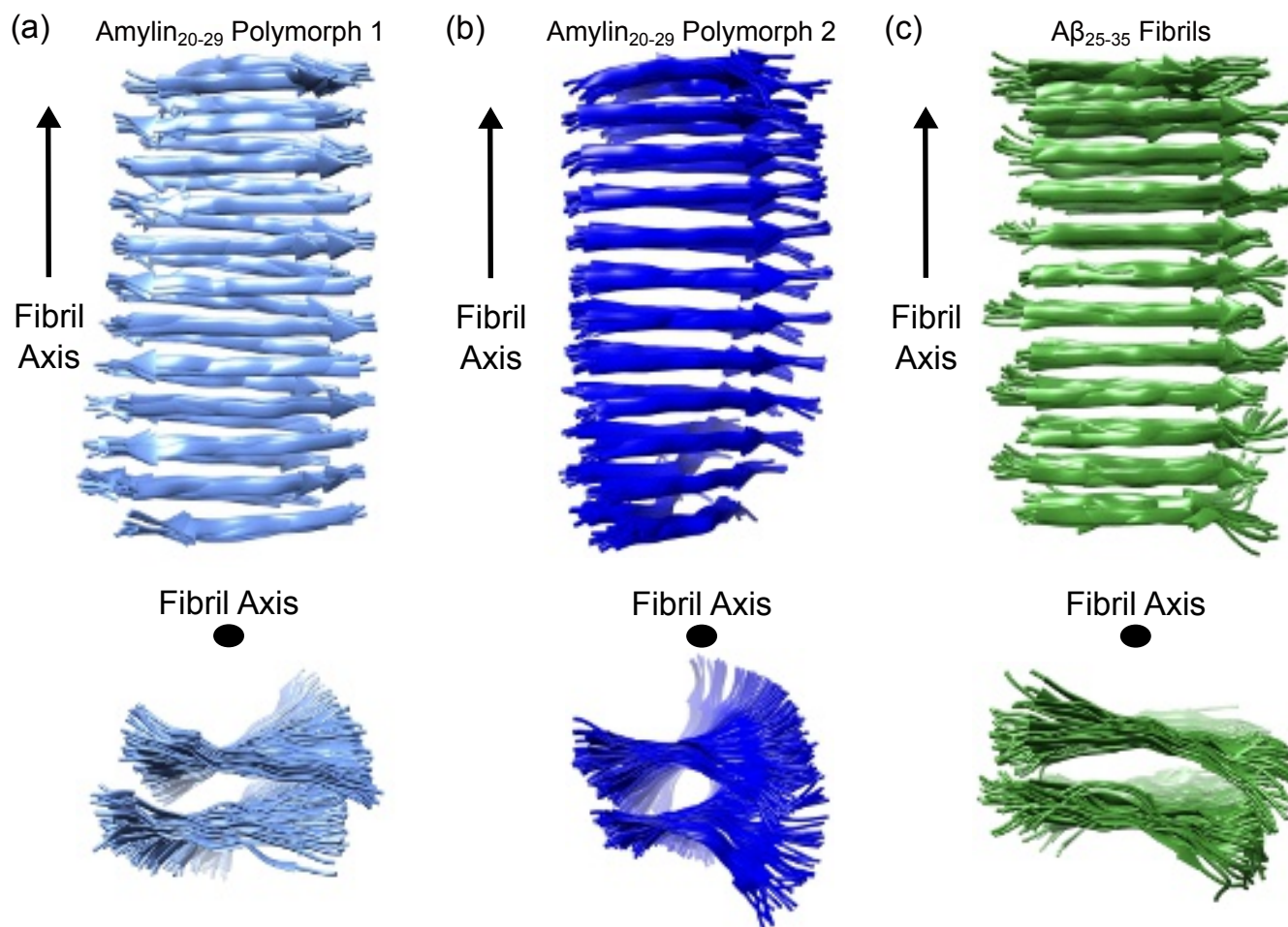


FIG. 8. Representative structural snapshots of fibrils obtained from MD simulations using Raman experimental constraints. (a) Amylin<sub>20–29</sub> polymorph 1. (b) Amylin<sub>20–29</sub> polymorph 2. (c) A $\beta$ <sub>25–35</sub> fibrils.

structures. For amylin<sub>20–29</sub> polymorph 1, hydrophobic contacts occur between the side chains of Phe, alanine (Ala), and

isoleucine (Ile) residues within the same  $\beta$ -sheet, while the side chains of leucine (Leu), Ala, and Ile form hydrophobic

zippers between  $\beta$ -sheets (Figure S18a).

In contrast, the side chains of Ala, Ile, and Leu residues are aligned down the length of the  $\beta$ -sheets for polymorph 2, forming a string of hydrophobic interactions between neighboring residues and hydrophobic zippers between opposite  $\beta$ -sheets, similar to polymorph 1 (Figure S18b and c). In addition, the side chains of Phe residues between neighboring  $\beta$ -strands in polymorph 2 form  $\pi$ -stacking interactions with each other. This constrains the Phe rings so that they adopt well-defined conformations, which is confirmed by the narrow bands observed for the Phe rings in the Raman spectrum shown in Figure 2b.

For  $A\beta_{25-35}$ , hydrophobic interactions occur between the side chains of Ala and Ile residues within the same  $\beta$ -sheet, as well as Leu and Ile residues from opposite  $\beta$ -sheets (Figure S19a). In addition, hydrogen bonding interactions are observed between Ser, Asn, and Lys residues between neighboring  $\beta$ -strands (Figure S19b).

All three polymorphs obtained from the MD simulation exhibit structural features that are physically reasonable for amyloid fibrils. The average inter-sheet distances for the three structures are between 9.4 – 10.4 Å, and the average inter-strand spacings are between 4.9 – 5.1 Å (Table S3). These values are in good agreement with the equatorial and meridional spacings observed in experimental fiber diffraction data of amyloid fibrils.<sup>96</sup> Similarly, no unrealistic bond angle distortions or steric clashes are observed, and the ( $\psi$ ,  $\phi$ ,  $\omega$ ) Ramachandran angles are all within allowed values (Table S4 – S6). As a result, we have greater confidence that the structural models shown in Figure 8 are physically reasonable.

To further validate the models, we examined whether the simulated fibrils were structurally stable. We tested this by removing the structural constraints on the fibril structures and then running additional simulations. The unconstrained structures held together during the simulation production runs and did not dissociate. The C=O bond distributions (Figure S20) of the unconstrained structures are bimodal, exhibiting peaks around  $\pm 10 - 15^\circ$  from the fibril axes, in good agreement with our experimental data. Similarly, the median values for the  $\psi$ -angle distributions (Figure S21) are close to our experimental measurements. The distribution of amylin<sub>20-29</sub> polymorph 1 is unimodal and peaked near  $147^\circ$ . In contrast, the distributions for amylin<sub>20-29</sub> polymorph 2 and  $A\beta_{25-35}$  appear bimodal, exhibiting a main peak around  $139^\circ$  (close to experimental measurements) and a smaller peak that is downshifted to ca.  $120^\circ$ . This indicates that the fibril structures corresponding to amylin<sub>20-29</sub> polymorph 2 and  $A\beta_{25-35}$  have both slightly evolved compared to the original constrained structures. The reason for these discrepancies is likely due to the limitations of our simulations since we could only model a single protofilament segment. We hypothesize that the structures we simulated are more conformationally flexible (thus allowing the  $\psi$ -angle distributions to evolve) since they are not subjected to lattice packing forces of multiple protofilaments that stabilize real amyloid fibrils.

## G. Comparison with Other Fibril Models

Early studies utilizing ssNMR and IR spectroscopy by Landsbury and Griffin<sup>52,53</sup> suggested that amylin<sub>20-29</sub> fibrils are composed of antiparallel  $\beta$ -sheet structures. These findings were later corroborated by Nielsen and coworkers<sup>54</sup> who also employed ssNMR to investigate the structure of amylin<sub>20-29</sub> fibrils. The Landsbury-Griffin-Nielsen studies, however, have been contradicted by others, who suggest that amylin<sub>20-29</sub> fibrils can also form parallel  $\beta$ -sheet structures. Middleton and coworkers<sup>36</sup> employed ssNMR and X-ray fiber diffraction to investigate amylin<sub>20-29</sub> fibrils. Their analysis of <sup>13</sup>C cross-polarization MAS and RR ssNMR data revealed that amylin<sub>20-29</sub> can form both parallel and antiparallel  $\beta$ -sheet fibril polymorphs, despite electron micrographs of their fibril samples appearing morphologically homogeneous. Similarly, Song *et al.*<sup>97</sup> published a recent cryo-EM study, which also suggests that amylin<sub>20-29</sub> fibrils can adopt parallel  $\beta$ -sheet structures.

Our work corroborates the findings of Middleton and coworkers<sup>36</sup> that amylin<sub>20-29</sub> forms both parallel and antiparallel  $\beta$ -sheet fibril polymorphs. Furthermore, the structures that we determine for both polymorphs exhibit hydrophobic zippers between the side chains of Leu, Ala, and Ile that are consistent with ssNMR data obtained by both the Middleton and Nielsen groups<sup>36,54</sup>. In addition, the  $\beta$ -sheets of both polymorphs also exhibit a slight twist around their fibril axes, in agreement with the antiparallel  $\beta$ -sheet structure reported by Nielsen and coworkers<sup>54</sup>. This agreement between our structural models and those derived from ssNMR data highlight the utility and complementary nature of using Raman spectroscopy to quantitatively assess the molecular structures of different amyloid fibrils.

Regarding  $A\beta_{25-35}$ , we are unaware of any detailed fibril structures being reported in the literature. In the case of the full-length (1 – 40 or 1 – 42) wildtype  $A\beta$  peptide, residues 25 – 29 adopt a bend structure that brings the two  $\beta$ -sheets of the fibril protofilaments together.<sup>18</sup> In contrast,  $A\beta_{25-35}$  is too small to adopt bend or turn structures. Its cross- $\beta$  core structure resembles that of amylin<sub>20-29</sub> polymorph 2. Interestingly,  $A\beta_{25-35}$  fibrils appear to be more structurally heterogeneous than amylin<sub>20-29</sub> polymorph 2 fibrils, as evidenced by the former's broader  $\psi$ -angle distribution (c.f. Figure 3b and c). This may be due to the difference in side chain composition of the two peptides. Amylin<sub>20-29</sub> polymorph 2 adopts parallel  $\beta$ -sheets that allows Phe, Ala, and Leu side chains to be aligned in-register between neighboring  $\beta$ -strands, thereby allowing hydrophobic and  $\pi$ -stacking interactions that make the fibril structures more rigid. The MD simulations suggest that this does not occur for  $A\beta_{25-35}$  fibrils since the side chains hydrophobic residues in the interior between the two  $\beta$ -sheets are more disordered (Figure S10). This side chain disordering could give rise to the greater conformational heterogeneity observed in the Raman spectra for  $A\beta_{25-35}$  fibrils compared to amylin<sub>20-29</sub> polymorph 2.

## V. CONCLUSION

In this study, we present detailed molecular-level structural models of amylin<sub>20–29</sub> and A $\beta$ <sub>25–35</sub> fibrils determined using MD simulations that are based on C=O bond and  $\psi$ -dihedral angle constraints measured by Raman spectroscopy. The agreement between our fibril models of amylin<sub>20–29</sub> polymorphs 1 and 2 with those reported by the Landsbury,<sup>52</sup> Griffin,<sup>53</sup> Middleton,<sup>36</sup> and Nielsen<sup>54</sup> groups highlight the potential to develop quantitative molecular structural models of fibrils using Raman spectroscopy. It also highlights the fact that our approach provides structural information that complements gold-standard techniques such as ssNMR and cryo-EM.

We believe that using experimental parameters measured by Raman spectroscopy to guide MD is more powerful and synergistic than using either technique alone. Namely, the bond and dihedral angle parameters measured by Raman spectroscopy provide structural constraints that help guide the construction of starting models and narrow the conformational phase space sampled over the course of the simulation production runs. In addition, the MD simulations provide a powerful method to visualize the three-dimensional structure of amyloid fibrils in a way that cannot be appreciated by only inspecting the bond and dihedral angle distributions measured by Raman spectroscopy. Finally, our work shows that Raman spectroscopy can be used to quantitatively discriminate between different fibril polymorphs.

We believe that our approach could be useful in refining fibril structures determined by ssNMR or cryo-EM. This is particularly true for refining disordered or dynamic regions of fibrils, which are difficult to probe using ssNMR and cryo-EM, that could play important roles in initiating aggregation or aberrantly interacting with biological cells. For ssNMR, the final ensemble of structures is visualized by selecting the top 10 or 20 most energetically favorable protein conformers consistent with the experimental constraints applied in the MD simulations. In cryo-EM, disordered, dynamic, or heterogeneous regions could result in poorly resolved electron densities that make it difficult to obtain any structural information at all. In contrast, the widths of dihedral and bond angle distributions measured by Raman spectroscopy naturally give insights into the structural dynamics and conformational heterogeneity of fibrils. This information can be directly incorporated into simulations by parameterizing MD force fields with experimentally measured harmonic force constants, as described above.

The Raman structural constraints used to parameterize the MD simulations can theoretically be determined using either non-polarized or polarized measurements. Although measuring the C=O bond angle distributions require polarization measurements on aligned samples, determining parameters such as  $\psi$ -dihedral angles with Raman spectroscopy does not. Thus, in theory, our approach does not inherently rely on aligned fibril samples or polarization measurements. However, for this to be feasible, more structurally-sensitive Raman spectroscopic markers need to be discovered to enable the determination of higher-resolution fibril models. There are

several reports describing Raman spectroscopic markers that can be used to measure amino acid side chain dihedral angles. However, these apply to only a handful of amino acids such as glutamine, asparagine, and tryptophan.<sup>21,24,25,98,99</sup> Discovering a Ramachandran  $\varphi$ -dihedral angle spectroscopic marker would be especially powerful for constraining the structure of the peptide backbone in fibrils. Work by Schweitzer-Stenner and coworkers<sup>100,101</sup> describes an interesting approach to analyze the Amide I band to determine both Ramachandran  $\psi$ - and  $\varphi$ - angles. However, it remains unclear whether their methodology can be applied to systems beyond tetrapeptides.

Obtaining site-specific structural information would also be useful in developing our technique. Residue-specific structural information could conceivably be obtained through site-specific labeling schemes of amide nitrogen and carbon atoms. Since the pathophysiologically-relevant lengths of many amyloidogenic proteins, including amylin, are generally less than 50 amino acids, isotopic editing of peptides could be achieved using solid-phase synthesis.<sup>70,102,103</sup> Isotopic labeling of the peptide backbone carbon and nitrogen atoms would decouple the NH bending, CN stretching, and C=O stretching motions in amide vibrations.<sup>81</sup> Isolating the corresponding Amide I and III modes for individual residues could therefore be achieved by determining the difference spectra between the isotopically labeled and unlabeled fibril species.<sup>81</sup> Thus, with these current limitations, it is clear that follow-up studies are needed to increase the utility of our methodology. Despite this, however, we believe that our approach lays a foundation towards potentially using Raman spectroscopy with MD to visualize the three-dimensional structures of amyloid fibrils and other biological macromolecules.

## SUPPLEMENTARY INFORMATION

Tables S1-S6 and Figures S1-S21. Description of additional Raman spectroscopy methods, spectral processing and peak-fitting methods, AFM methods, FTIR methods, and determination of Ramachandran  $\psi$ -angle distribution and order parameters.

## ACKNOWLEDGEMENT

We thank Rusul Mustafa, Lauren Aheran, Dr. Kateryna Friedman, and Prof. Daniel Moriarty for useful discussions. We thank Nicole Bouffard for her support with AFM. Funding for this work was provided by the University of Vermont, the Spectroscopy Society of Pittsburgh (DP and MH), and the National Institutes of Health (P20 GM1350007) through the Vermont Center for Cardiovascular and Brain Health pilot grant award (DP, YO, MH, and UN). The Raman microscope used in this work was purchased from funds provided by the National Science Foundation (DMR-1919610). The AFM used in this work was purchased from funds provided by the National Center for Research Resources (S10RR025498).

## AUTHOR DECLARATIONS

## Conflict of Interest

The authors have no conflicts to disclose.

## Author Contributions

**Madeline Harper:** Conceptualization (supporting); Formal analysis (equal); Investigation (lead); Methodology (equal); Software (equal); Validation (lead); Visualization (lead); Writing - original draft (lead); Writing - review & editing (equal). **Uma Nudurupati:** Formal analysis (supporting); Investigation (supporting); Methodology (supporting); Visualization (supporting); Writing - review & editing (supporting). **Riley J. Workman:** Formal analysis (supporting); Investigation (supporting); Methodology (supporting); Writing - review & editing (supporting). **Taras I. Lakoba:** Formal analysis (supporting); Software (equal); Writing - review & editing (supporting). **Nicholas Perez:** Investigation (supporting). **Delaney Nelson:** Investigation (supporting). **Yang-guang Ou:** Funding acquisition (equal); Resources (supporting); Supervision (supporting); Writing - review & editing (equal). **David Punihale:** Conceptualization (lead); Formal analysis (equal); Funding acquisition (equal); Methodology (equal); Project Administration (lead); Resources (lead); Software (lead); Supervision (lead); Visualization (equal); Writing - review & editing (lead).

## DATA AVAILABILITY

The data that support the findings of this study are available from the corresponding author upon reasonable request.

## REFERENCES

- <sup>1</sup>F. Chiti and C. M. Dobson, "Protein misfolding, functional amyloid, and human disease," *Annu. Rev. Biochem.* **75**, 333–366 (2006).
- <sup>2</sup>R. Tycko and R. B. Wickner, "Molecular structures of amyloid and prion fibrils: Consensus versus controversy," *Acc. Chem. Res.* **46**, 1487–1496 (2013).
- <sup>3</sup>Q. Cao, D. R. Boyer, M. R. Sawaya, P. Ge, and D. S. Eisenberg, "Cryo-EM structure and inhibitor design of human IAPP (amylin) fibrils," *Nat. Struct. Mol. Biol.* **27**, 653–659 (2020).
- <sup>4</sup>R. Gallardo, M. G. Iadanza, Y. Xu, G. R. Heath, R. Foster, S. E. Radford, and N. A. Ranson, "Fibril structures of diabetes-related amylin variants reveal a basis for surface-templated assembly," *Nat. Struct. Mol. Biol.* **27**, 1048–1056 (2020).
- <sup>5</sup>C. Röder, T. Kupreichyk, L. Gremer, L. U. Schäfer, K. R. Pothula, R. B. G. Ravelli, D. Willbold, W. Hoyer, and G. F. Schröder, "Cryo-EM structure of islet amyloid polypeptide fibrils reveals similarities with amyloid- $\beta$  fibrils," *Nat. Struct. Mol. Biol.* **27**, 660–667 (2020).
- <sup>6</sup>M. D. Tuttle, G. Comellas, A. J. Nieuwkoop, D. J. Covell, D. A. Berthold, K. D. Kloepper, J. M. Courtney, A. M. Kim, J. K. and Barclay, A. Kendall, W. Wan, G. Stubbs, C. D. Schwieters, V. M. Y. Lee, J. M. George, and C. M. Rienstra, "Solid-state NMR structure of a pathogenic fibril of full-length human  $\alpha$ -synuclein," *Nat. Struct. Mol. Biol.* **23**, 409–415 (2016).

- <sup>7</sup>W. Qiang, W.-M. Yau, J.-X. Lu, J. Collinge, and R. Tycko, "Structural variation in amyloid- $\beta$  fibrils from Alzheimer's disease clinical subtypes," *Nature* **541**, 217–221 (2017).
- <sup>8</sup>M. Kollmer, W. Close, L. Funk, J. Rasmussen, A. Bsoul, A. Schierhorn, M. Schmidt, C. J. Sigurdson, M. Jucker, and M. Fändrich, "Cryo-EM structure and polymorphism of A $\beta$  amyloid fibrils purified from Alzheimer's brain tissue," *Nat. Commun.* **10**, 4760 (2019).
- <sup>9</sup>Q. Cao, D. R. Boyer, M. R. Sawaya, R. Abskharon, L. Saelices, J. Nguyen, B. A. and Lu, K. A. Murray, and D. S. Kandeel, F. and Eisenberg, "Cryo-EM structures of hIAPP fibrils seeded by patient-extracted fibrils reveal new polymorphs and conserved fibril cores," *Nat. Struct. Mol. Biol.* **28**, 724–730 (2021).
- <sup>10</sup>U. Ghosh, K. R. Thurber, W.-M. Yau, and R. Tycko, "Molecular structure of a prevalent amyloid- $\beta$  fibril polymorph from Alzheimer's disease brain tissue," *Proc. Natl. Acad. Sci. U.S.A.* **118**, e2023089118 (2021).
- <sup>11</sup>Y. Yang, D. Arseni, W. Zhang, M. Huang, S. Lövestam, M. Schweighauser, A. Kotecha, A. G. Murzin, S. Y. Peak-Chew, J. Macdonald, I. Lavenir, H. J. Garringer, E. Gelpi, K. L. Newell, G. G. Kovacs, R. Vidal, B. Ghetti, B. Ryskeldi-Falcon, S. H. W. Scheres, and M. Goedert, "Cryo-EM structures of amyloid- $\beta$  42 filaments from human brains," *Science* **375**, 167–172 (2022).
- <sup>12</sup>M. Lee, W.-M. Yau, J. M. Louis, and R. Tycko, "Structures of brain-derived 42-residue amyloid- $\beta$  fibril polymorphs with unusual molecular conformations and intermolecular interactions," *Proc. Natl. Acad. Sci. U.S.A.* **120**, e2218831120 (2023).
- <sup>13</sup>L. C. Serpell, "Alzheimer's amyloid fibrils: structure and assembly," *Biochim. Biophys. Acta Mol. Basis Dis.* **1502**, 16–30 (2000).
- <sup>14</sup>R. Tycko, "Molecular structure of amyloid fibrils: insights from solid-state NMR," *Q. Rev. Biophys.* **39**, 1–55 (2006).
- <sup>15</sup>R. Tycko, "Physical and structural basis for polymorphism in amyloid fibrils," *Protein Sci.* **23**, 1528–1539 (2014).
- <sup>16</sup>R. Tycko, "Amyloid polymorphism: Structural basis and neurobiological relevance," *Neuron* **86**, 632–645 (2015).
- <sup>17</sup>R. Tycko, "Solid-state NMR studies of amyloid fibril structure," *Annu. Rev. Phys. Chem.* **62**, 279–299 (2011).
- <sup>18</sup>A. T. Petkova, Y. Ishii, J. J. Balbach, O. N. Antzutkin, R. D. Leapman, F. Delaglio, and R. Tycko, "A structural model for Alzheimer's  $\beta$ -amyloid fibrils based on experimental constraints from solid state NMR," *Proc. Natl. Acad. Sci. U.S.A.* **99**, 16742–16747 (2002).
- <sup>19</sup>J. D. Flynn, R. P. McGlinchey, I. Walker, R. L., and J. C. Lee, "Structural features of  $\alpha$ -synuclein amyloid fibrils revealed by Raman spectroscopy," *J. Biol. Chem.* **293**, 767–776 (2018).
- <sup>20</sup>N. C. Maiti, M. M. Apetri, M. G. Zagorski, P. R. Carey, and V. E. Anderson, "Raman spectroscopic characterization of secondary structure in natively unfolded proteins:  $\alpha$ -synuclein," *J. Am. Chem. Soc.* **126**, 2399–2408 (2004).
- <sup>21</sup>D. Punihale, R. J. Workman, Z. Hong, J. D. Madura, and S. A. Asher, "Polyglutamine fibrils: New insights into antiparallel  $\beta$ -sheet conformational preference and side chain structure," *J. Phys. Chem. B* **120**, 3012–3026 (2016).
- <sup>22</sup>V. Sereda, M. R. Sawaya, and I. K. Lednev, "Structural organization of insulin fibrils based on polarized Raman spectroscopy: Evaluation of existing models," *J. Am. Chem. Soc.* **137**, 11312–11320 (2015).
- <sup>23</sup>L. A. Popova, R. Kodali, R. Wetzel, and I. K. Lednev, "Structural variations in the cross- $\beta$  core of amyloid  $\beta$  fibrils revealed by deep UV resonance Raman spectroscopy," *J. Am. Chem. Soc.* **132**, 6324–6328 (2010).
- <sup>24</sup>D. Punihale, Z. Hong, R. S. Jakubek, E. M. Dahlburg, S. Geib, and S. A. Asher, "Glutamine and asparagine side chain hyperconjugation-induced structurally sensitive vibrations," *J. Phys. Chem. B* **119**, 13039–13051 (2015).
- <sup>25</sup>D. Punihale, R. S. Jakubek, R. J. Workman, L. E. Marbella, P. Campbell, J. D. Madura, and S. A. Asher, "Monomeric polyglutamine structures that evolve into fibrils," *J. Phys. Chem. B* **121**, 5953–5967 (2017).
- <sup>26</sup>V. Sereda and I. K. Lednev, "Polarized Raman spectroscopy of aligned insulin fibrils," *J. Raman Spectrosc.* **45**, 665–671 (2014).
- <sup>27</sup>M. M. Apetri, N. C. Maiti, M. G. Zagorski, P. R. Carey, and V. E. Anderson, "Secondary structure of  $\alpha$ -synuclein oligomers: Characterization by Raman and Atomic Force Microscopy," *J. Mol. Biol.* **355**, 63–71 (2006).
- <sup>28</sup>P. Westermark, C. Wernstedt, E. Wilander, and K. Sletten, "A novel peptide in the calcitonin gene related peptide family as an amyloid fibril pro-

- tein in the endocrine pancreas," *Biochem. Biophys. Res. Commun.* **140**, 827–831 (1986).
- <sup>29</sup>G. J. Cooper, A. Willis, A. Clark, R. Turner, R. Sim, and K. Reid, "Purification and characterization of a peptide from amyloid-rich pancreases of type 2 diabetic patients." *Proc. Natl. Acad. Sci. U.S.A.* **84**, 8628–8632 (1987).
- <sup>30</sup>P. Westermark, C. Wernstedt, E. Wilander, D. Hayden, T. O'Brien, and K. Johnson, "Amyloid fibrils in human insulinoma and islets of langerhans of the diabetic cat are derived from a neuropeptide-like protein also present in normal islet cells." *Proc. Natl. Acad. Sci. U.S.A.* **84**, 3881–3885 (1987).
- <sup>31</sup>P. Westermark, A. Andersson, and G. T. Westermark, "Islet amyloid polypeptide, islet amyloid, and diabetes mellitus," *Physiol. Rev.* **91**, 795–826 (2011).
- <sup>32</sup>C. A. Jurgens, M. N. Toukatly, C. L. Fligner, J. Udayasankar, S. L. Subramanian, S. Zraika, K. Aston-Mourney, D. B. Carr, P. Westermark, G. T. Westermark, S. E. Kahn, and R. L. Hull, " $\beta$ -cell loss and  $\beta$ -cell apoptosis in human type 2 diabetes are related to islet amyloid deposition," *Am. J. Pathol.* **178**, 2632–2640 (2011).
- <sup>33</sup>K. Rajasekhar, M. Chakrabarti, and T. Govindaraju, "Function and toxicity of amyloid beta and recent therapeutic interventions targeting amyloid beta in Alzheimer's disease," *Chem. Commun.* **51**, 13434–13450 (2015).
- <sup>34</sup>J. Attems, K. Jellinger, D. R. Thal, and W. Van Nostrand, "Review: Sporadic cerebral amyloid angiopathy," *Neuropathol. Appl. Neurobiol.* **37**, 75–93 (2011).
- <sup>35</sup>Y. Masahito, "Cerebral amyloid angiopathy: Emerging concepts," *J. Stroke* **17**, 17–30 (2015).
- <sup>36</sup>J. Madine, E. Jack, P. G. Stockley, S. E. Radford, L. C. Serpell, and D. A. Middleton, "Structural insights into the polymorphism of amyloid-like fibrils formed by region 20–29 of amylin revealed by solid-state NMR and X-ray fiber diffraction," *J. Am. Chem. Soc.* **130**, 14990–15001 (2008).
- <sup>37</sup>R. D. Deegan, O. Bakajin, T. F. Dupont, G. Huber, S. R. Nagel, and T. A. Witten, "Capillary flow as the cause of ring stains from dried liquid drops." *Nature* **389**, 827–829 (1997).
- <sup>38</sup>F. Adar, "Raman polarization measurements: Keeping track of the instrumental components' behavior," <https://www.spectroscopyonline.com> (2017), accessed: August 2, 2022.
- <sup>39</sup>A. Raj, C. Kato, H. A. Witek, and H.-o. Hamaguchi, "Toward standardization of Raman spectroscopy: Accurate wavenumber and intensity calibration using rotational Raman spectra of H<sub>2</sub>, HD, D<sub>2</sub>, and vibration-rotation spectrum of O<sub>2</sub>," *J. Raman Spectrosc.* **51**, 2066–2082 (2020).
- <sup>40</sup>J. Allkins and E. Lippincott, "Raman polarization measurements on liquids using 180°, He/Ne laser excitation—the skeletal bending modes of acetone and acetone-d<sub>6</sub>," *Spectrochim. Acta A Mol. Biomol. Spectrosc.* **25**, 761–764 (1969).
- <sup>41</sup>V. Ostapchenko, M. Gasset, and I. V. Baskakov, "Atomic force fluorescence microscopy in the characterization of amyloid fibril assembly and oligomeric intermediates," *Methods Mol. Biol.* **849**, 156–167 (2012).
- <sup>42</sup>W. Humphrey, A. Dalke, and K. Schulten, "VMD: Visual molecular dynamics," *J. Mol. Graph.* **14**, 33–38 (1996).
- <sup>43</sup>J. Huang and A. D. MacKerell Jr, "CHARMM36 all-atom additive protein force field: Validation based on comparison to NMR data," *J. Comput. Chem.* **34**, 2135–2145 (2013).
- <sup>44</sup>J. Huang, S. Rauscher, G. Nawrocki, R. Ting, M. Feig, B. de Groot, H. Grubmüller, and A. MacKerell, "CHARMM36m: An improved force field for folded and intrinsically disordered proteins," *Biophys. J.* **112**, 175a–176a (2017).
- <sup>45</sup>T. Darden, D. York, and L. Pedersen, "Particle mesh Ewald: An N-log(N) method for Ewald sums in large systems," *J. Chem. Phys.* **98**, 10089–10092 (1993).
- <sup>46</sup>D. A. Case, T. E. Cheatham III, T. Darden, H. Gohlke, R. Luo, K. M. Merz Jr., A. Onufriev, C. Simmerling, B. Wang, and R. J. Woods, "The Amber biomolecular simulation programs," *J. Comput. Chem.* **26**, 1668–1688 (2005).
- <sup>47</sup>D. R. Roe and T. E. Cheatham, "PTRAJ and CPPTRAJ: Software for processing and analysis of molecular dynamics trajectory data," *J. Chem. Theory Comput.* **9**, 3084–3095 (2013).
- <sup>48</sup>D. F. Moriarty and D. P. Raleigh, "Effects of sequential proline substitutions on amyloid formation by human amylin<sub>20–29</sub>," *Biochemistry* **38**, 1811–1818 (1999).
- <sup>49</sup>P. Westermark, U. Engström, K. Johnson, G. Westermark, and C. Betsholtz, "Islet amyloid polypeptide: pinpointing amino acid residues linked to amyloid fibril formation." *Proc. Natl. Acad. Sci. U.S.A.* **87**, 5036–5040 (1990).
- <sup>50</sup>G. G. Glenner, E. D. Eanes, and C. A. Wiley, "Amyloid fibrils formed from a segment of the pancreatic islet amyloid protein," *Biochem. Biophys. Res. Commun.* **155**, 608–614 (1988).
- <sup>51</sup>R. Hajiraissi, I. Giner, G. Grundmeier, and A. Keller, "Self-assembly, dynamics, and polymorphism of hIAPP(20–29) aggregates at solid-liquid interfaces," *Langmuir* **33**, 372–381 (2017).
- <sup>52</sup>T. T. Ashburn, M. Auger, and P. T. Lansbury, "The structural basis of pancreatic amyloid formation: isotope-edited spectroscopy in the solid state," *J. Am. Chem. Soc.* **114**, 790–791 (1992).
- <sup>53</sup>J. M. Griffiths, T. T. Ashburn, M. Auger, P. R. Costa, R. G. Griffin, and P. T. J. Lansbury, "Rotational resonance solid-state NMR elucidates a structural model of pancreatic amyloid," *J. Am. Chem. Soc.* **117**, 3539–3546 (1995).
- <sup>54</sup>J. T. Nielsen, M. Bjerring, M. D. Jeppesen, R. O. Pedersen, J. M. Pedersen, K. L. Hein, T. Vosegaard, T. Skrydstrup, D. E. Otzen, and N. C. Nielsen, "Unique identification of supramolecular structures in amyloid fibrils by solid-state NMR spectroscopy," *Angew. Chem. Int. Ed.* **48**, 2118–2121 (2009).
- <sup>55</sup>L. Millucci, L. Ghezzi, G. Bernardini, and A. Santucci, "Conformations and biological activities of amyloid beta peptide 25–35," *Curr. Protein Pept. Sci.* **11**, 54–67 (2010).
- <sup>56</sup>Y. Song, P. Li, C. Liu, L. and Bortolini, and M. Dong, "Nanostructural differentiation and toxicity of amyloid- $\beta$ 25–35 aggregates ensue from distinct secondary conformation," *Sci. Rep.* **8**, 765 (2018).
- <sup>57</sup>K. Sato, A. Wakamiya, T. Maeda, K. Noguchi, A. Takashima, and K. Imaehori, "Correlation among secondary structure, amyloid precursor protein accumulation, and neurotoxicity of amyloid $\beta$ (25–35) peptide as analyzed by single alanine substitution," *J. Biochem.* **118**, 1108–1111 (1995).
- <sup>58</sup>T. Konno, "Amyloid-induced aggregation and precipitation of soluble proteins: An electrostatic contribution of the Alzheimer's  $\beta$ (25–35) amyloid fibril," *Biochemistry* **40**, 2148–2154 (2001).
- <sup>59</sup>G. Shanmugam and R. Jayakumar, "Structural analysis of amyloid  $\beta$  peptide fragment (25–35) in different microenvironments," *Peptide Sci.* **76**, 421–434 (2004).
- <sup>60</sup>S. A. Asher, M. Ludwig, and C. R. Johnson, "UV resonance Raman excitation profiles of the aromatic amino acids," *J. Am. Chem. Soc.* **108**, 3186–3197 (1986).
- <sup>61</sup>W. H. Moore and S. Krimm, "Vibrational analysis of peptides, polypeptides, and proteins. II.  $\beta$ -poly(l-alanine) and  $\beta$ -poly(l-alanyl-glycine)," *Biopolymers* **15**, 2465–2483 (1976).
- <sup>62</sup>A. V. Mikhonin, S. V. Bykov, N. S. Myshakina, and S. A. Asher, "Peptide secondary structure folding reaction coordinate correlation between UV Raman Amide III frequency,  $\psi$  Ramachandran angle, and hydrogen bonding," *J. Phys. Chem. B* **110**, 1928–1943 (2006).
- <sup>63</sup>A. Barth, "Infrared spectroscopy of proteins," *Biochim. Biophys. Acta Bioenerg.* **1767**, 1073–1101 (2007).
- <sup>64</sup>A. Barth, "The infrared absorption of amino acid side chains," *Prog. Biophys. Mol. Biol.* **74**, 141–173 (2000).
- <sup>65</sup>W. H. Moore and S. Krimm, "Vibrational analysis of peptides, polypeptides, and proteins. I. polyglycine I," *Biopolymers* **15**, 2439–2464 (1976).
- <sup>66</sup>A. Savitzky and M. J. E. Golay, "Smoothing and differentiation of data by simplified least squares procedures," *Anal. Chem.* **36**, 1627–1639 (1964).
- <sup>67</sup>S. Krimm and Y. Abe, "Intermolecular interaction effects in the Amide I vibrations of  $\beta$  polypeptides," *Proc. Natl. Acad. Sci. U.S.A.* **69**, 2788–2792 (1972).
- <sup>68</sup>Y. Abe and S. Krimm, "Normal vibrations of crystalline polyglycine I," *Biopolymers* **11**, 1817–1839 (1972).
- <sup>69</sup>W. H. Moore and S. Krimm, "Transition dipole coupling in Amide I modes of  $\beta$  polypeptides," *Proc. Natl. Acad. Sci. U.S.A.* **72**, 4933–4935 (1975).
- <sup>70</sup>S. D. Moran and M. T. Zanni, "How to get insight into amyloid structure and formation from infrared spectroscopy," *J. Phys. Chem. Lett.* **5**, 1984–1993 (2014).
- <sup>71</sup>A. Barth and C. Zscherp, "What vibrations tell about proteins," *Q. Rev. Biophys.* **35**, 369–430 (2002).
- <sup>72</sup>T. Miyazawa, "Perturbation treatment of the characteristic vibrations of polypeptide chains in various configurations," *J. Chem. Phys.* **32**, 1647–

- 1652 (1960).
- <sup>73</sup>T. Miyazawa and E. R. Blout, "The infrared spectra of polypeptides in various conformations: Amide I and II bands," *J. Am. Chem. Soc.* **83**, 712–719 (1961).
- <sup>74</sup>R. W. Williams and A. Dunker, "Determination of the secondary structure of proteins from the Amide I band of the laser Raman spectrum," *J. Mol. Biol.* **152**, 783–813 (1981).
- <sup>75</sup>Y. Wang, R. Purrello, S. Georgiou, and T. G. Spiro, "UVRaman spectroscopy of the peptide bond. 2. Carbonyl H-bond effects on the ground- and excited-state structures of N-methylacetamide," *J. Am. Chem. Soc.* **113**, 6368–6377 (1991).
- <sup>76</sup>H. Torii, T. Tatsumi, T. Kanazawa, and M. Tasumi, "Effects of intermolecular hydrogen-bonding interactions on the Amide I mode of N-methylacetamide: Matrix-isolation infrared studies and ab initio molecular orbital calculations," *J. Phys. Chem. B.* **102**, 309–314 (1998).
- <sup>77</sup>W. R. W. Welch, J. Kubelka, and T. A. Keiderling, "Infrared, vibrational circular dichroism, and Raman spectral simulations for  $\beta$ -sheet structures with various isotopic labels, interstrand, and stacking arrangements using density functional theory," *J. Phys. Chem. B.* **117**, 10343–10358 (2013).
- <sup>78</sup>D. Punihaole, R. S. Jakubek, E. M. Dahlburg, Z. Hong, N. S. Myshakina, S. Geib, and S. A. Asher, "UV resonance Raman investigation of the aqueous solvation dependence of primary Amide vibrations," *J. Phys. Chem. B* **119**, 3931–3939 (2015).
- <sup>79</sup>Y. Kuroda, Y. Saito, K. Maghida, and T. Uno, "Vibrational spectra of propionamide and its C- and N-deuterated compounds," *Bull. Chem. Soc. Jpn.* **45**, 2371–2383 (1972).
- <sup>80</sup>X. G. Chen, S. A. Asher, R. Schweitzer-Stenner, N. G. Mirkin, and S. Krimm, "UV Raman determination of the  $\pi\pi^*$  excited state geometry of N-methylacetamide: Vibrational enhancement pattern," *J. Am. Chem. Soc.* **117**, 2884–2895 (1995).
- <sup>81</sup>A. V. Mikhonin, Z. Ahmed, A. Ianoul, and S. A. Asher, "Assignments and conformational dependencies of the Amide III peptide backbone UV resonance Raman bands," *J. Phys. Chem. B* **108**, 19020–19028 (2004).
- <sup>82</sup>S. A. Asher, A. Ianoul, G. Mix, M. N. Boyden, A. Karnoup, M. Diem, and R. Schweitzer-Stenner, "Dihedral  $\psi$  angle dependence of the Amide III vibration: A uniquely sensitive UV resonance Raman secondary structural probe," *J. Am. Chem. Soc.* **123**, 11775–11781 (2001).
- <sup>83</sup>J. M. Dudik, C. R. Johnson, and S. A. Asher, "UV resonance Raman studies of acetone, acetamide, and N-methylacetamide: models for the peptide bond," *J. Phys. Chem.* **89**, 3805–3814 (1985).
- <sup>84</sup>D. Punihaole, R. S. Jakubek, R. J. Workman, and S. A. Asher, "Interaction enthalpy of side chain and backbone Amides in polyglutamine solution monomers and fibrils," *J. Phys. Chem. Lett.* **9**, 1944–1950 (2018).
- <sup>85</sup>S. A. Asher, A. V. Mikhonin, and S. Bykov, "UV Raman demonstrates that  $\alpha$ -helical polyalanine peptides melt to polyproline II conformations," *J. Am. Chem. Soc.* **126**, 8433–8440 (2004).
- <sup>86</sup>J. S. Richardson, in *The Anatomy and Taxonomy of Protein Structure*, Advances in Protein Chemistry, Vol. 34 (Academic Press, 1981) pp. 167–339.
- <sup>87</sup>Q. Li, Y. T. Zhu, I. A. Kinloch, and A. H. Windle, "Self-organization of carbon nanotubes in evaporating droplets," *J. Phys. Chem. B* **110**, 13926–13930 (2006).
- <sup>88</sup>M. Tsuboi, J. M. Benevides, and G. J. Thomas Jr., "Raman tensors and their application in structural studies of biological systems," *Proc. Jpn. Acad., Ser. B* **85**, 83–97 (2009).
- <sup>89</sup>M.-E. Rousseau, T. Lefèvre, L. Beaulieu, T. Asakura, and M. Pézolet, "Study of protein conformation and orientation in silkworm and spider silk fibers using Raman microspectroscopy," *Biomacromolecules* **5**, 2247–2257 (2004).
- <sup>90</sup>F. L. Labarthe, T. Buffeteau, and C. Sourisseau, "Orientation distribution functions in uniaxial systems centered perpendicularly to a constraint direction," *Appl. Spectrosc.* **54**, 699–705 (2000).
- <sup>91</sup>H. Pottel, W. Herreman, B. van der Meer, and M. Ameloot, "On the significance of the fourth-rank orientational order parameter of fluorophores in membranes," *Chem. Phys.* **102**, 37–44 (1986).
- <sup>92</sup>B. J. Berne, P. Pechukas, and G. D. Harp, "Molecular reorientation in liquids and gases," *J. Chem. Phys.* **49**, 3125–3129 (1968).
- <sup>93</sup>D. I. Bower, "Orientation distribution functions for uniaxially oriented polymers," *J. Polym. Sci. Polym. Phys. Ed.* **19**, 93–107 (1981).
- <sup>94</sup>W. L. Jorgensen, J. Chandrasekhar, J. D. Madura, R. W. Impey, and M. L. Klein, "Comparison of simple potential functions for simulating liquid water," *J. Chem. Phys.* **79**, 926–935 (1983).
- <sup>95</sup>M. Amin and J. Küpper, "Variations in proteins dielectric constants," *ChemistryOpen* **9**, 691–694 (2020).
- <sup>96</sup>M. Sunde and C. C. Blake, "From the globular to the fibrous state: protein structure and structural conversion in amyloid formation," *Q. Rev. Biophys.* **31**, 1–39 (1998).
- <sup>97</sup>Y. Song, B. Dai, Y. Wang, Y. Wang, C. Liu, P. Gourdon, L. Liu, K. Wang, and M. Dong, "Identifying heterozyper  $\beta$ -sheet in twisted amyloid aggregation," *Nano Lett.* **22**, 3707–3712 (2022).
- <sup>98</sup>T. Miura, H. Takeuchi, and I. Harada, "Tryptophan Raman bands sensitive to hydrogen bonding and side-chain conformation," *J. Raman Spectrosc.* **20**, 667–671 (1989).
- <sup>99</sup>T. Maruyama and H. Takeuchi, "Effects of hydrogen bonding and side-chain conformation on the Raman bands of tryptophan-2,4,5,6,7-d<sub>5</sub>," *J. Raman Spectrosc.* **26**, 319–324 (1995).
- <sup>100</sup>R. Schweitzer-Stenner, F. Eker, Q. Huang, and K. Griebenow, "Dihedral angles of trialanine in D<sub>2</sub>O determined by combining FTIR and polarized visible Raman spectroscopy," *J. Am. Chem. Soc.* **123**, 9628–9633 (2001).
- <sup>101</sup>F. Eker, K. Griebenow, X. Cao, L. A. Nafie, and R. Schweitzer-Stenner, "Preferred peptide backbone conformations in the unfolded state revealed by the structure analysis of alanine-based (AXA) tripeptides in aqueous solution," *Proc. Natl. Acad. Sci. U.S.A.* **101**, 10054–10059 (2004).
- <sup>102</sup>D. B. Strasfeld, Y. L. Ling, R. Gupta, D. P. Raleigh, and M. T. Zanni, "Strategies for extracting structural information from 2D IR spectroscopy of amyloid: Application to islet amyloid polypeptide," *J. Phys. Chem. B.* **113**, 15679–15691 (2009).
- <sup>103</sup>S.-H. Shim, R. Gupta, Y. L. Ling, D. B. Strasfeld, D. P. Raleigh, and M. T. Zanni, "Two-dimensional IR spectroscopy and isotope labeling defines the pathway of amyloid formation with residue-specific resolution," *Proc. Natl. Acad. Sci. U.S.A.* **106**, 6614–6619 (2009).